

Scattering and absorption of a bosonic field impinging on a charged black hole in the Einstein-Maxwell-dilaton theory

Martín G. Richarte,^{1,2,3,a} Ébano L. Martins,^{1,b} and Júlio C. Fabris^{2,4,5,c}

¹*Departamento de Física - Universidade Federal do Espírito Santo, 29075-910 Vitória, ES, Brazil*

²*PPGCosmo, CCE - Universidade Federal do Espírito Santo, 29075-910 Vitória, ES, Brazil*

³*Departamento de Física, Facultad de Ciencias Exactas y Naturales,*

Universidad de Buenos Aires, Ciudad Universitaria 1428, Pabellón I, Buenos Aires, Argentina

⁴*Núcleo Cosmo-ufes&Departamento de Física - Universidade Federal do Espírito Santo, 29075-910 Vitória, ES, Brazil*

⁵*National Research Nuclear University MEPhI, Kashirskoe sh. 31, Moscow 115409, Russia*

(Dated: June 10, 2022)

In this study, we revisit the absorption and scattering process by which a massless bosonic field impinges on a charged dilatonic black hole. Using the partial wave method, we determine numerically the total absorption cross-section in terms of the decoupling parameter called $M\omega$, finding that the amplitude of the dilatonic black hole is lower than the Reissner-Nordström one for mild frequencies. In the limit of high-frequency, the absorption cross-section exhibits two different kinds of complex behaviors, one is referred to as the fine structure and the other as the hyperfine structure. To fully grasp the main properties of the charged dilatonic black hole, we consider a different framework where the compact object is impinged by a charged massive bosonic field. In the low-frequency limit, we argue that the absorption cross-section presents two different phases, which are indicated by the value of a critical velocity. Depending on the dark matter model and the black hole mass, we show that both phases are relevant. We verify that the superradiance scattering takes place, being enhanced by smaller scalar field mass but larger values of the scalar field charge. For intermediate frequency, the superradiant effect is lessened in relation to the Reissner-Nordström case. However, this effect does not necessarily imply the existence of any instability. In order to trigger the superradiant instability, two conditions must be met. There must be unstable modes that remain trapped outside the event horizon with a mechanism based on the reflecting-mirror boundary conditions. This mechanism allows for the system composed of a charged scalar field plus a charged black hole to produce a charged black hole bomb. We provide an analytic formula (lower bound) for the values of the charge field which can trigger this superradiant instability.

CONTENTS

		B. Superradiant instability	23
I. Introduction	1	VII. Conclusions	26
II. EMd theory	3	Acknowledgments	27
III. Classical analysis	4	A. Penrose diagram	27
IV. Massless Scalar Field	7	B. Logarithmic approximation for the backward glory effect	28
A. Absorption cross-section	8	References	29
B. Numerical results for absorption	9		
C. Scattering cross-section	10		
D. Absorption cross-section for high energies	12		
V. Charged massive scalar field	14		
A. Low-frequency regime	16		
B. high-frequency	20		
C. Numerical results for scattering	21		
VI. Superradiant scattering	22		
A. Numerical results	22		

I. INTRODUCTION

General Relativity (GR) admits the existence of several kinds of compact objects such as stars and black holes. The latter ones are the final stage of a star that has collapsed in on itself. They have such a strong gravitational field that it pulls in everything within their surrounding environments: gas, interstellar dust, and even light [1], [2], [3]. These astrophysical objects have been detected by different telescopes/satellites and other ground-based devices [5]. The first indirect detection of black hole in astrophysics goes back to 1964 when a powerful source of X-ray was detected in Earth

^a martin@df.uba.ar~ (corresponding author)

^b ebano.lm@gmail.com

^c julio.fabris@cosmo-ufes.org

coming from a distant constellation called Cygnus [4]. Since then, the evidences supporting the existence of black holes in the Universe have been increasing at an amazing pace, specially for the last 30 years [5]. In particular, the first detection by the LIGO interferometer of a gravitational wave signal produced by the merging of two black holes in 2015 is considered as a strong confirmation of GR [6]. In 2019, the first image of the surrounding of black hole at the center of a massive galaxy in the nearby Virgo galaxy cluster, Messier 87*, was obtained by the EHT collaboration [7]. Both collaborations are sources of new findings about black hole properties (mass, spin) and its environments (accretion disk).

Among the most simplest generalizations of GR, there is a class of frameworks in which, besides the Hilbert-Einstein term, the additional degree of freedoms are minimally coupled to gravity. One of the most popular one is the so-called Einstein-Maxwell-dilaton (EMd) gravity where a scalar field (dilaton) is coupled to the kinetic term of a gauge $U(1)$ field. In addition to the kinetic term associated with the dilaton field, a self-interacting potential could be included. Historically speaking, the EMd gravity emerges as the bosonic sector of $SU(4)$ version of $N = 4$ supergravity theory but it also appears in the low-energy limit of the heterotic string as an effective theory [8], [9]. The recent interest in the black hole solutions within the EMd gravity relies on the fact that, besides the mass and charge parameter, the dilaton field adds a new charge to the theory. So the question is whether the dilaton field is radiated away from the black hole or if this global charge persists, evading the no-hair conjecture that states that a black is only characterized by its mass, charge and angular momentum [1]-[2]. This point is still debatable provided it depends on the way that the dilaton field is coupled to the gauge field along with the extremality character of the black hole [10]. The violation of the no-hair conjecture has been explored in different setups. In the case of EM gravity plus a self-interacting scalar field, not coupled to the gauge field, a comparison between the shadow produced by a black hole with hair and the shadow of M87* obtained by the Event Horizon Telescope led to strong constraints on the breaking of the no-hair conjecture [11]. Moreover, the possibility of observing in Nature hairy black holes in EMd framework was confronted with the waveform of gravitational waves generated by a binary system [12], [13]. Similar results on the contribution of the gravitational waves signal within the PPN formalism for binary black holes in EMd gravity were reported in [14], [15].

Another appealing reason for exploring the EMd gravity is that the theory does not seem to disobey the weak cosmic censorship conjecture. In another words, the electrically charged black hole with non-zero dilaton charge can not be destroyed (overcharged or over-spun) provided the second order perturbations intro-

duce a backreaction effect, preventing in this way the exposure of a naked singularity [16], [17]. The viability of the EMd theory at the Solar system level and its contrast with the four classical experiments of GR were reported in [18], [19]. For an extension of EMd theory, an extra scalar field (axion) can be added. Performing a Bayesian analysis with the data collected by the X-ray telescopes, that is the emission of X-ray coming from the accreting material around black holes [21], was possible to open a complementary window to constrain the spacetime around X-ray binary system with low mass.

It is worth stressing at this point that there are alternative ways to understand the properties of the spacetime associated to a black hole solution. Almost fifty-three year ago Matzner explored the process by which a massless scalar field hit a black hole; a fraction of the initial wave is absorbed and the other fraction is scattered off [22]. In his seminal work, Matzner obtained the scattering cross-section in the zero frequency limit showing that the total cross-section for the absorption process vanishes [22]. A central concept in deriving the aforesaid result is the determination of those null geodesics near the black hole which are absorbed or scattered off; those possibilities depend on the value given to the initial impact parameter. The deflection angle by which the null geodesics are deflected or not around the black hole does not have a closed form, and for that reason, this quantity is calculated in weak field limit. As result of this approach an approximated expression for the differential cross-section is obtained [22]. The main contribution for small angle depends quadratically on the black hole's mass [22], [23]. For Schwarzschild black hole a detailed analysis of the absorption cross-section associated with different values of energy and angular momentum was carried out by Sanchez several years later [24]. The scattering of gravitational radiation by Schwarzschild black hole was also explored [25]. In 2004, Jun and Park performed a full analysis on the role played by a massive scalar field in the absorption and emission spectra of Schwarzschild black hole [28].

An interesting phenomenon that appears when of massless scalar wave hits a black hole and scatters off is known as glory effect and it was originally explored by Matzner, Dewitt-Morette, Nelson and Zhang in 1985 [26]. If the outgoing scattered wave is close to the direction of the initial incoming wave an interference process takes place, creating a pattern in which the black center is surrounded by a bright halo [26]. Further studies showed that the forward glory is a considerably small effect in black holes [27]. The analysis of backward glory effect was extended to other black hole solutions. For instance, the scattering and absorption of massless scalar field by a Reissner-Nordström black hole was explored by Crispino, Dolan and Oliveira in 2009 [29]. They applied the partial wave method to calculate cross-sections and also showed a good agreement with the numerically-calculated total cross-sections. One interesting point is

that the effects coming from the charge are not always subdominant with respect to black hole's mass. The differential cross-section revealed a subdominant contribution, however, the cross-section at large angle and the width of the glory peak are both quite sensible with the charge of the black hole [29]. The scattering of electromagnetic wave by a Schwarzschild black hole was explored by the same authors [30]. Since these seminal works, the typical pattern produced by the scattering of wave with a black hole has been used as a powerful tool to extract properties of black hole. The scattering/absorption process of wave by a black hole was examined in the case a canonical acoustic black hole [31], a charged black hole [32], [33], dirty black holes [34], Kerr black holes [35], charged dilatonic black hole [36], and for black hole in Hovara-Lifshitz gravity [37]. The absorption of s -waves by a remanent black hole within in metric-affine gravity was explored by Delhom *et al.* [38].

These facts motivate the exploration of both the process of scattering and absorption of massless scalar wave by a charged dilaton black hole, extending previous analysis [36]. In Sec. II we introduce the EMD gravity and the charged dilatonic black hole, including the Penrose diagram for the charged black hole, which later is fully explained in Appendix A. One of the goals of this study is to determine the classical differential cross-section for massless scalar field and to explore the backward glory effect numerically for different value of the dimensionless charge, q . The latter part is covered in Sec. III and in the Appendix B a semi-analytic approach to examine the glory effect is contrasted with the full numerical differential cross-section along with the differential cross-section of the backward glory effect. Sec. IVA is devoted to obtain the absorption cross-section by means of the partial wave method. In Sec. IVB, we numerically compare the pattern associated with the total absorption cross-section in terms of the dimensionless coupling $M\omega$ [29] for different values of q . In addition to that, we employ a numerical integration method which allows us to reconstruct the differential scattering cross-section for different values of $M\omega$ and q , as is shown in Sec. IVC. One way to improve the previous analysis is by looking at the behavior of the absorption cross-section of massless scalar field in the limit of high energy [39], [40], [41], [42]. In Sec. IVD, our aim is to obtain the absorption cross-section in the limit of high-frequency. The numerical analysis reveals the existence of different complex structures in the total absorption cross-section, also known as the fine and hyperfine structures [42]. In Sec. V, we extend the studies on the absorption of a charged massive boson field by a charged dilatonic black hole; including a full analysis on the behavior of the cross-section in the limit of low and high-frequency. In Sec. VA, the findings in the low-frequency regime are confirmed by numerical simulations which point out that the existence of

two different phases and a critical velocity parameter, v_c , indicating the transition between both stages. To measure the relevance of these numerical analysis, we inspect several models of dark matter—with their typical average velocity v_X and masses m_X — and determine for different kinds of black holes (stellar, intermediate, supermassive, primordial) the critical velocity parameter, and by doing so, we conclude whether these models are compatible with a subcritical phase $v_X \ll v_c$ or a supercritical phase $v_X \gg v_c$. In Sec.VB, we employ numerical simulations to obtain the cross-section in the high energy limit, but only for the massive scalar field case, showing how the geometric contribution is essentially corrected by some oscillatory behavior. In Sec. VC, the numerical simulations for the differential scattering cross-section are displayed. In Sec. VIA, the reflection coefficient is obtained, finding that there is a superradiant phenomenon and extending previous results on the literature [36],[43], [44]. In Sec. VIB, we explore whether the superradiant scattering implies the existence of superradiant instability, showing that the unstable modes lead to instability if exists a well potential outside the horizon where these modes remain enclosed. Moreover, we obtain there is a lower bound on the eq quantity in order to the instability happens, and the reflecting-mirror boundary condition provides the proper mechanism to the system mirror plus black hole to become a charged black hole bomb. Finally, the conclusions are stated in Sec. VII.

Throughout this paper we use geometric units so that $c = 1$, $\hbar = 1$, $G = 1$. The metric signature is mostly positive, $(-, +, +, +)$.

II. EMD THEORY

As we stated before, EMD gravity is an effective theory appearing in the low-energy limit of the heterotic superstring model [8], [9]. Besides the graviton as part of the particle content of the theory, there is a gauge field and a scalar field, whereas the abelian gauge field and dilaton are coupled minimally to gravity, they both coupled to each other in a non-trivial way controlled by an exponential term, its action reads

$$S = \frac{1}{16\pi} \int d^4x \sqrt{-g} \{ R - 2\partial_\mu \phi \partial^\mu \phi - e^{-2\phi} F_{\mu\nu} F^{\mu\nu} \}, \quad (1)$$

where $F_{\mu\nu} = \partial_\mu A_\nu - \partial_\nu A_\mu$ is the electromagnetic tensor. The variation of the action (1) with respect to $g^{\mu\nu}$, A_μ and ϕ results in the following equation of motion,

$$R_{\mu\nu} = 2\partial_\mu \phi \partial_\nu \phi + 2e^{-2\phi} \left(F_{\mu\beta} F_\nu^\beta - \frac{1}{4} g_{\mu\nu} F^2 \right), \quad (2)$$

$$\nabla_\nu (e^{-2\phi} F^{\mu\nu}) = 0, \quad (3)$$

$$\nabla_\mu \nabla^\mu \phi = -\frac{1}{2} e^{-2\phi} F^2. \quad (4)$$

This theory allows the existence of black hole solutions which are for asymptotically flat. These solutions describe regular black holes with a non-degenerate event horizon and were obtained by Gibbons and Maeda 33 years ago[45]. In the case of electrostatic solution, the metric and matter fields are given by

$$ds^2 = -f(r)dt^2 + \frac{1}{f(r)}dr^2 + r^2g(r)d\Omega^2, \quad (5)$$

$$e^{2\phi} = e^{2\phi_\infty}g(r), \quad (6)$$

$$F = \frac{Q}{r^2}e^{\phi_\infty}dr \wedge dt, \quad (7)$$

$$g(r) = \left(1 - \frac{2D}{r}\right), \quad (8)$$

$$f(r) = \frac{(r - 2M)}{r} \quad (9)$$

where ϕ_∞ is the value of ϕ at infinity. Besides, the mass M and the electric charge Q the addition of the dilaton introduces a new global quantity called dilatonic charge [46]. This charge is calculated as

$$D = \frac{1}{4\pi} \lim_{r \rightarrow \infty} \oint d\Sigma^\mu \partial_\mu \phi \approx \frac{Q^2}{2M}, \quad (10)$$

where the 2-volume form is $d\Sigma_\alpha = \eta_\alpha \sqrt{-h} d^3x$ and $\eta_\alpha = f^{1/2}(0, 1, 0, 0)$ is the normal vector to the surface Σ ($||\eta^\mu|| = -1$).

The case with $M > 0$ represents a black hole with a spacelike singularity hidden by the event horizon which is located at $r_h = 2M$. Notice that this charged black hole solution does not present two horizons as is the case with Reissner-Nordström black hole. Additionally, the area of the sphere goes to zero for $r = 2D$ so this surface becomes singular. In $D \simeq M$ limit, a relationship between the electric charge and mass parameter is obtained, namely, $Q^2 = 2M^2$. In this way, it is admissible to re-write the equations only in terms of the parameters Q and M . Now the singular surface area is reached if the condition $r = Q^2/M$ is met. For $Q < \sqrt{2}M$ the singularity is hidden by the event horizon; see the Penrose diagram depicted in Fig.(1), but is fully explained in the Appendix A. We will consider the black hole with the parameters satisfying the condition $Q^2 \leq 2M^2$. In the extreme case, $Q = \sqrt{2}M$, the singularity coincides with the horizon [47], [46]. As is expected, the zero electric charged condition ($Q = 0$) leads to the Schwarzschild solution. However, the comparison with Reissner-Nordström is elusive provided there is no values of Q which gives back the RN metric [46]. Regarding this last point, we must emphasize that the comparison with the charged black hole in GR must be done with some care otherwise we will end up misinterpreting our findings.

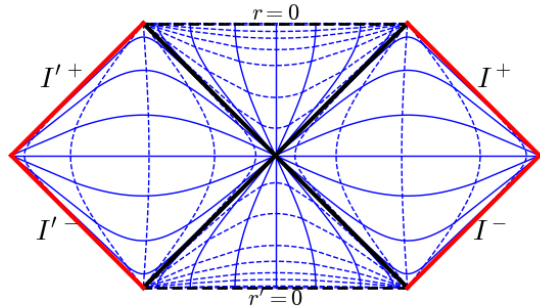


Figure 1: Penrose diagram for the charged black hole in EMd theory. The bold black line corresponds to the event horizon and the dashed black line corresponds to the spacelike singularity.

III. CLASSICAL ANALYSIS

In this section we will determine the absorption differential cross-section working within the short-wavelength approximation ($\lambda \ll r_h$), so it is sufficient to visualize plane waves as rays associated with the null geodesics [36]. To do so, we begin by exploring the behavior of null geodesic in terms of the impact parameter. Our first task is to obtain the critical impact parameter as the distance within photons are captured by the compact object [1]. As usual, the null geodesics for the metric (5) are described by

$$g_{\mu\nu} \dot{x}^\mu \dot{x}^\nu = 0, \quad (11)$$

where $\dot{x}^\mu = dx^\mu/d\lambda$ is the four-velocity and λ stands for the affine parameter. Since the static spacetime has two Killing vectors, ∂_t and ∂_ϕ , this implies the existence of two conserved quantities, namely the energy ($E = f(r)dt/d\lambda$) and angular momentum ($L = r^2 \sin^2 \theta d\phi/d\lambda$). A full analysis of the geodesics for dilatonic black holes is reported in [48]. In the case of null geodesics in the equatorial plane ($\theta = \pi/2$), replacing the metric (5) in (11) we arrive at an effective problem with a radial equation and angular velocity given by

$$\begin{aligned} \dot{r}^2 &= E^2 - \frac{L^2}{r^2} f, \\ \Omega &= \frac{\dot{\phi}}{\dot{t}} = \frac{L}{E} \frac{f}{r^2}, \end{aligned} \quad (12)$$

so that the orbital equation can be recast as

$$\left(\frac{du}{d\varphi}\right)^2 = h(u), \quad (13)$$

$$h(u) = (1 - 2q^2u)^2 \left[\frac{1}{\bar{b}^2} - \left(\frac{1 - 2u}{1 - 2q^2u} \right) u^2 \right],$$

where $u = M/r$, $b = L/E$, and $\bar{b} = M/b$ is a dimensionless inverse impact parameter. The critical radius,

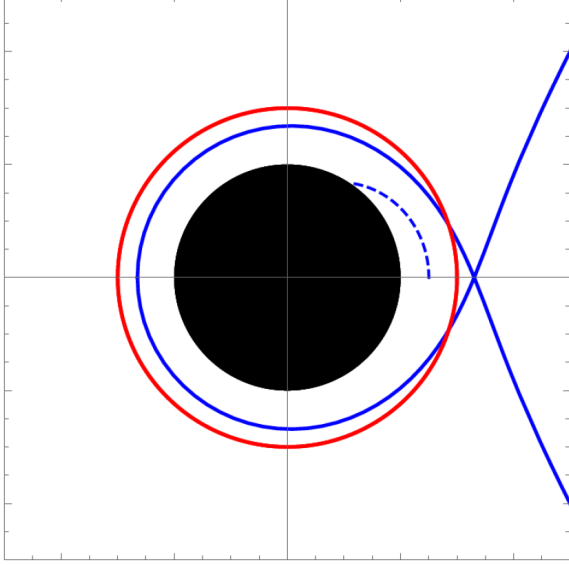


Figure 2: Null geodesics around dilaton black hole for $M = 1$ and $q = 0.3$.

$u_c = M/r_c$, can be found by solving $h'(u) = 0$. We then substitute the value of u_c into Eq.(13) and solve $h(u_c) = 0$ to find the possible values of b_c corresponding to a non-deflected geodesic. Applying this procedure we end up with the following critical value:

$$\frac{b_c}{M} = \sqrt{\frac{27 - q^4 - 18q^2 + (9 - q^2) \sqrt{(1 - q^2)(9 - q^2)}}{2}}, \quad (14)$$

where $q^2 = Q^2/(2M^2)$ represents a dimensionless charge. A photon will be scattered off for $b > b_c$, otherwise it will be absorbed by the black hole [see Fig. (2)]. In fact, the critical impact parameter can be obtained by taking into account a physical situation where the photon coming from the infinity is trapped in an **unstable** circular orbit with radius r_c around the black hole; this case is achieved if the following conditions are met (12): $1 - E^2/L^2 = f_c/(g_c r_c^2)$, $2 - 2f_c g_c' = r_c g_c f_c'$, and $3 - 2f_c < r_c^2 (f_c''/g_c')$. Consequently, the photon which is scattered by the compact object and goes back to infinity has an angle of deflection [36] given by

$$\Theta(b) = 2 \int_0^{u_0} \frac{du}{\sqrt{h(u)}} - \pi. \quad (15)$$

It is possible to solve the above expression analytically for $\Theta(b)$ in the weak-field limit ($b \gg M$):

$$\Theta \approx \frac{4M}{b} + \frac{\wp(q)M^2}{b^2}, \quad (16)$$

where $\wp(q) = (3\pi/4)(5 - 4q^2 - \frac{4}{3}q^4)$. For $q = 0$, we recover the well-known Einstein formula for the deflection of light, $\Theta \approx 4M/b$ [1], at the leading order

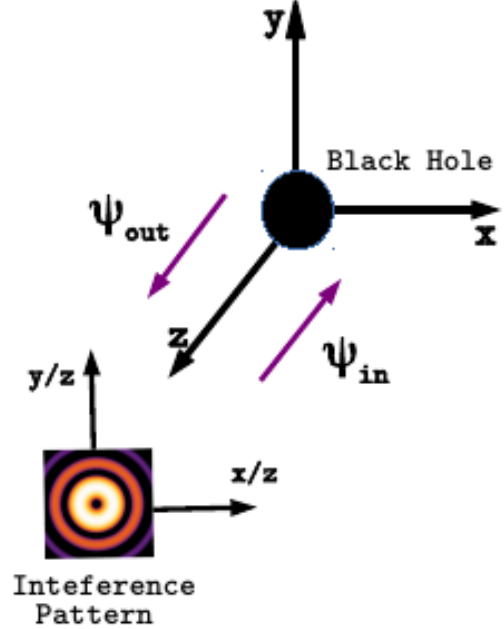


Figure 3: Schematic representation of the backward glory effect.

within the weak-field approximation. However, this expression is different from the one obtained in the case of Reissner–Nordström black hole [29], where $\wp(q)$ becomes a quadratic polynomial at order $(M/b)^2$.

Having obtained the critical impact parameter for the deflected null geodesics, we are in position to calculate the differential cross-section [23], [29], which reads

$$\frac{d\sigma}{d\Omega} = \frac{b}{\sin \Theta} \left| \frac{db}{d\Theta} \right|. \quad (17)$$

To obtain (17) we make use of the approximated deflection angle (16). The classical differential cross-section for small angles becomes

$$\frac{d\sigma}{d\Omega} \simeq \frac{16M^2}{\Theta^4} + \frac{M^2}{\Theta^3} \wp(q). \quad (18)$$

The dominant term in the classical scattering formula neither depend on q nor the deflection angle does. The situation also happened with the Reissner–Nordström metric. Once again, the comparison with the Reissner–Nordström black hole leads to a mismatch even if the quartic term is neglected from the above formula. We conclude that the null geodesics are less sensible to q for small Θ they provided only see a black hole with mass M [29]. At intermediate deflection angles, the null geodesics notice a charged black hole with mass M and charge Q .

Since part of the incoming wave is scattered off by the black hole, at some point along the line-of-sight, it

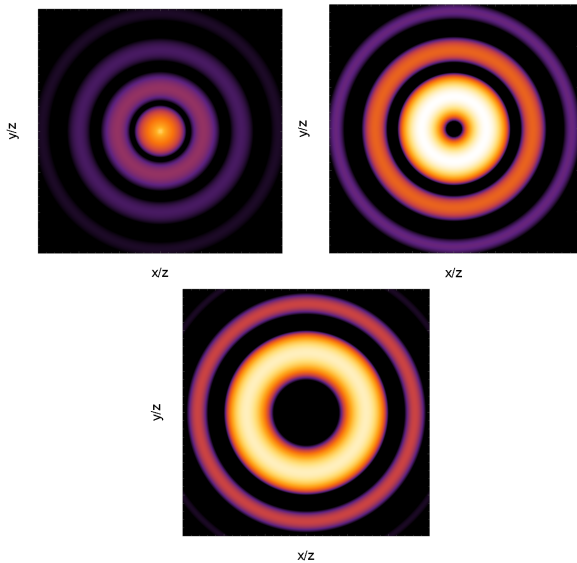


Figure 4: Illustration of the glory effect for charged dilatonic black holes for spins $s = \{0, 1, 2\}$ and decoupling parameter $M\omega = 15$.

is expected that the outgoing wave interferes with the incoming wave, generating a pattern of bright fringes around a black center [26] (see Fig. 3). This mechanism is known as glory effect and can be used to extract physical properties of the black hole near of the horizon [26], [29]. A full derivation of the differential cross-section can be derived using a path integral approach [26], and it reads:

$$\left. \frac{d\sigma}{d\Omega} \right|_{\Theta \simeq \pi} \simeq 2\pi\omega b_g^2 \left| \left. \frac{db}{d\Theta} \right|_{\Theta \simeq \pi} [J_{2s}(\omega b_g \sin \Theta)]^2 \right|^2, \quad (19)$$

where b_g is the impact parameter for the geodesics that undergo a 180° deflection and $J_{2s}(x)$ is the Bessel function of first type whereas its order $2s$ indicates the particle's spin, s . There are several values of b_g corresponding to the number of times the photon has completed a loop around the black hole, i.e., for each deflection angle $\Theta = \pi + 2\pi n$, where n is an integer. This approximation remains valid as long as the high-frequency regime ($M\omega \gg 1$) holds. Fig.(4) illustrates a typical profile describing the backward glory effect as detected by a distant observer from the Emd black hole. For zero spin, constructive interference happens for $\theta = 180^\circ$, which is represented by a white center. This feature is also noted in the Schwarzschild black hole [26]. The case of an electromagnetic wave impinging upon a black hole was explored in detailed by Crispino, Dolan and Oliveira [30], and by doing so, they obtained the full numerical differential cross-section for electromagnetic waves, comparing to the approximated version calculated for the glory effect [30]. In Fig. (5) we show the differential cross-section associated with the glory effect in the of charged dilatonic black hole which are asymptot-

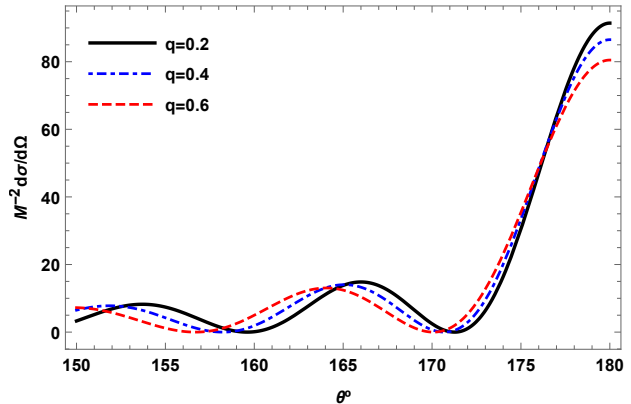


Figure 5: Differential cross-section of the dilatonic black hole for $M\omega = 3$ taking into account the glory effect.

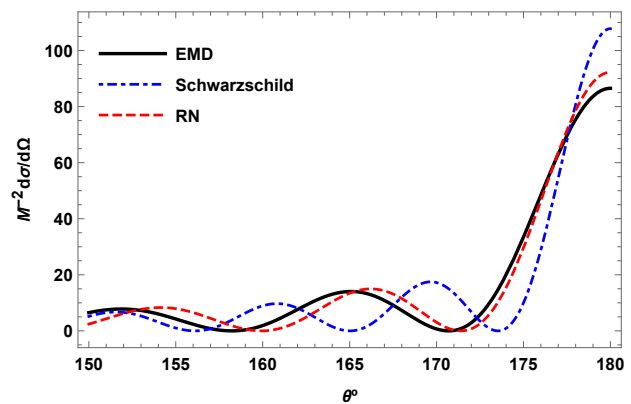


Figure 6: Glory effect comparison in terms of the differential scattering cross-section of Schwarzschild, Reissner-Nordström, and dilatonic charged black holes for $q = 0.3$ and $M\omega = 3$.

ically flat within the Emd model. For different values of the dimensionless charge, q , the pattern corresponds to an oscillatory function which increases its amplitudes as the angle reaches the critical value $\theta_c = 180^\circ$. All cases exhibit the same kind of profile in terms of the angle; that is, a series of oscillation produced by the interference of rays in opposite directions very close to each other. Depending on the value of n the pattern exhibits a bright or black fringes. In fact, smaller values of q lead to larger amplitudes. The comparison of the glory effect among the Schwarzschild black hole, Reissner-Nordström metric and dilatonic black holes is depicted in Fig.(6). The Reissner-Nordström and dilatonic black holes have very near curves and they both have a smaller differential cross-section in relation to the Schwarzschild black hole, specially the amplitude peak around $\theta_c = 180^\circ$. In order to arrive at an order of magnitude for the differential cross-section in the case of glory effect (19), we proceed to determine first the impact parameter for the glory

q	b_g/M	$\left. \frac{b_g^2}{M^2} \frac{db}{d\theta} \right _{\theta \sim \pi}$
0	5.36	4.89
0.2	5.28	4.85
0.4	4.96	4.59
0.6	4.65	4.27
0.8	3.96	3.59
1	2.06	2.21

Table I: Impact parameter for the glory effect.

effect called b_g and the rate $\frac{db}{d\theta}$. We start by fixing M and Q , or equivalently q , and then we obtain b_g by solving numerically the condition $\Theta(b_g) = \pi$ with the help of (15). In table (I), we show different values of b_g and $\frac{db}{d\theta}$ for several values of q . Larger values of q yield to smaller value of b_g/M , and consequently, smaller value of dimensionless cross-section. Further, it is possible to obtain an approximated expression for the deflection angle which leads to a semi-analytic formula for estimating the magnitude and width of the glory peak for the dilatonic charged black hole (see Appendix B).

IV. MASSLESS SCALAR FIELD

So far we have been working within the short-wavelength approximation ($\lambda \ll r_h$) so it was useful for visualizing the behavior of wave as rays (geometric optic), represented by null geodesics. In this section, we are going to apply a different approach to calculate the differential cross-section for scattering/absorption process. This requires to employ the so-called partial wave method for intermediate wavelengths ($\lambda \simeq r_h$). Hence, we consider an incoming wave from infinity, which is partially transmitted through the event horizon and partially scattered to infinity [30], [35]. To study that we write down the Klein-Gordon equation of a massless scalar field propagating on the dilatonic black hole background,

$$\square \Phi = \frac{1}{\sqrt{|g|}} \partial_\mu \left(\sqrt{|g|} g^{\mu\nu} \partial_\nu \Phi \right) = 0, \quad (20)$$

where \square is the Laplace-Beltrami operator on curved spacetime $\mathcal{M} = \mathbb{R} \times \Sigma_3$ and g is the metric determinant. It is convenient to mention that the solutions of (20) have associated an inner Klein-Gordon product defined by [2],[3]

$$\Omega(\Phi, \Psi) = \int_{\Sigma_3} d\Sigma_\mu J^\mu, \quad (21)$$

where the invariant volume form is defined as $d\Sigma_\mu = \sqrt{|h|} n_\mu \Sigma_3 dx^3$, h is the determinant of the induced met-

ric on the Cauchy surface Σ_3 , and n_μ a unit vector time-like. There is a conserved current [3]

$$J_\mu = \frac{i}{2} [\Phi^* \nabla_\mu \Psi - \Psi^* \nabla_\mu \Phi], \quad (22)$$

its components include the number density of the field, J^t , along with the current densities, J^i . The general solution to equation (20) for the spherically symmetric dilatonic charged black hole background can be found using the separation of variables method, that is, we propose the following ansatz

$$\Phi = \sum_{\ell=0}^{\infty} \sum_{|m| \leq \ell} \int_{\mathbb{R}} \frac{\psi_{\ell m \omega}(r)}{r \sqrt{g(r)}} Y_{\ell m}(\theta, \varphi) e^{-i\omega t} d\omega, \quad (23)$$

where $Y_\ell^m(\theta, \phi) : \mathbb{S}^2 \rightarrow \mathbb{C}$ are the spherical harmonics, and ω is the frequency. The spacetime variables cover the exterior of black hole, namely, $2M < r < \infty$, $0 < t < \infty$, $0 \leq \theta \leq 2\pi$ and $0 \leq \phi \leq \pi$. Substituting (23) in (20) we obtain the master equation for the radial solution $\psi_{\ell m \omega}$

$$f(r) \left(f(r) \psi'_{\ell m \omega} \right)' + (\omega^2 - V(r)) \psi_{\ell m \omega} = 0, \quad (24)$$

where the prime stands for derivated w.r.t. the radial coordinate. In fact, we introduce a tortoise coordinate defined by the relation $dx = f(r)^{-1} dr$, so that the map between these radial coordinates reads

$$x = \int \frac{dr}{f(r)} = r + 2M \ln \left| \frac{r}{2M} - 1 \right|. \quad (25)$$

The tortoise coordinate covers the real line interval, that is, the boundaries of the radial interval correspond to the following asymptotics: $x(2M) \rightarrow -\infty$ and $x(\infty) \rightarrow -\infty$. Replacing (25) in (24), we arrive at a more appealing master equation which resembles the Schrödinger one for stationary states with energy $E = \omega^2$:

$$-\frac{d^2}{dx^2} \psi_{\ell m \omega}(x) + V(r) \psi_{\ell m \omega}(x) = \omega^2 \psi_{\ell m \omega}(x). \quad (26)$$

The effective potential is given by

$$M^2 V(r) = \left(1 - \frac{2}{r} \right) \left[\frac{\ell(\ell+1)}{r^2 - 2q^2 r} - \frac{q^4 \left(1 - \frac{2}{r} \right)}{r^4 \left(1 - \frac{2q^2}{r} \right)^2} + \frac{2q^2}{r^4 \left(1 - \frac{2q^2}{r} \right)} + \frac{2}{r^3} \right]. \quad (27)$$

As the radial coordinate approaches at the horizon the effective potential (27) vanishes and the same happens at infinity. In Fig.(7), we show that the effective potential exhibits a bell-shaped curve in the tortoise coordinate for different values of the angular momentum and for a fixed charge-to-mass ratio $q = 0.5$. It is clear

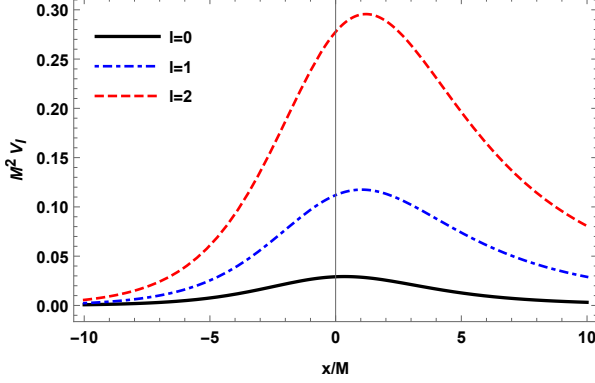


Figure 7: Effective potential for the massless scalar field in the dilatonic charged black hole case as a function of the tortoise coordinate for fixed $q = 0.5$ and different values of ℓ .

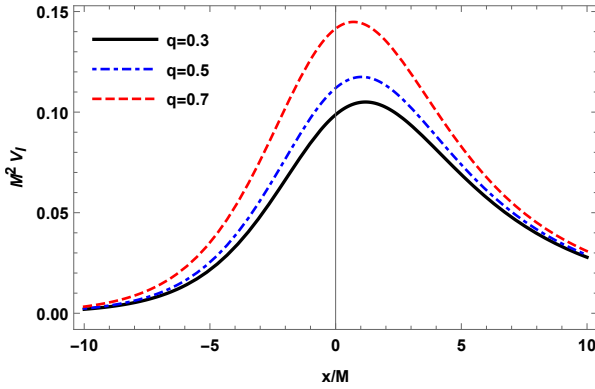


Figure 8: Effective potential for the massless scalar field in the dilatonic charged black hole case as a function of the tortoise coordinate for fixed $\ell = 1$ and different values of q

from Fig.(8) that for a given ℓ the height of the peak increases as q takes larger values.

Notice that the radial solutions $\psi_{\ell m \omega}$ inherit a set of orthonormality conditions coming from inner KG product for orthonormal solution (21),

$$\Omega(\psi_{\ell m \omega}, \psi_{\ell' m' \omega'}) = \delta_{\ell \ell'} \delta_{m m'} \delta(\omega - \omega') \quad (28)$$

$$\Omega(\psi_{\ell m \omega}^*, \psi_{\ell' m' \omega'}) = 0. \quad (29)$$

A. Absorption cross-section

Since we are dealing with a boundary value problem for the Schrödinger equation (26) with an effective potential (27), a key point is the selection of the boundary conditions for the radial solution $\psi_{\ell m \omega}(x)$ which are compatible with the problem at hand. Close to the horizon, $r = 2M$, the effective potential vanishes and the boundary condition is that radial function mode must

be represented by an ingoing wave

$$\psi_{\omega \ell} \simeq A_{\omega \ell} T_{\omega \ell} e^{-i\omega x}, \quad (30)$$

where $A_{\omega \ell}$ is a normalization constant and $|T_{\omega \ell}|$ is called the transmission coefficient. The index m is omitted for simplicity. As we consider the opposite limit the dominant contribution of the effective potential is the angular barrier, $\ell(\ell + 1)/r^2$. Eq.(24) can be written as

$$\left[r^2 \frac{d^2}{dr^2} + r \frac{d}{dr} + \omega^2 - \left(\ell + \frac{1}{2} \right)^2 \right] \left(\frac{\psi_{\omega \ell}}{\sqrt{\omega r}} \right) = 0, \quad (31)$$

which coincides with the Bessel equation of order $(\ell + 1/2)$, whose solution is given in terms of third order spherical Bessel functions $h_l(\omega r)$,

$$\psi_{\omega \ell} \simeq A_{\omega \ell}(\omega r) \left[(-i)^{\ell+1} h_\ell^*(\omega r) + i^{\ell+1} R_{\omega \ell} h_\ell(\omega r) \right]. \quad (32)$$

The factor $|R_{\omega \ell}|$ represents the reflection coefficient. The relationship between the transmission and reflection coefficients is the usual one: $|R_{\omega \ell}|^2 + |T_{\omega \ell}|^2 = 1$. Using that the leading order of the spherical Bessel function is [49]-[50]:

$$h_\ell(\omega r) \simeq (-i)^{\ell+1} \frac{e^{i\omega r}}{\omega r}, \quad (33)$$

then the asymptotic boundary condition becomes

$$\psi_{\omega \ell}(x) = A_{\omega \ell} \left(R_{\omega \ell} e^{i\omega x} + e^{-i\omega x} \right) \quad (34)$$

as long as we are in the region $\omega x \geq \ell(\ell + 1)/2$. Notice that the above approach for imposing the proper boundary conditions is consistent with the scattering of massless scalar field with reflective boundary condition at infinity and the one-way membrane at the horizon. In other words, our approach is consistent with previous works on this topic [29], [34], [38].

It is instructive, at this point, to determine the behavior of the radial modes in the limit of low-frequency, $\omega = 0$, also known as zero modes. Replacing the latter condition in Eq. (24), the general solution can be recast as [49]-[50]

$$\psi_{\omega \ell}(z) = D_{\omega \ell}^I P_\ell(z) + D_{\omega \ell}^{II} Q_\ell(z), \quad (35)$$

where the new variable is

$$z = \frac{1 + q^2 - \frac{r}{M}}{q^2 - 1} \quad (36)$$

In Eq. (35), $P_\ell(z)$ and $Q_\ell(z)$ are Legendre functions of first and second type [49]-[50], respectively. At the event horizon ($z = 1$) the asymptotic behavior of the Legendre functions are characterized by $Q_\ell(1) \rightarrow \infty$ and $P_\ell(1) = 1$ [49]. The radial modes at low-frequency that come from infinity must clearly represent the main contribution in the region and a subdominant fraction

at the horizon, this means that the modes coming from the infinity are given by the $P_\ell(z)$ function,

$$\psi_{\omega\ell}(z) = D_{\omega\ell}^I r \sqrt{2g(r)} P_\ell(z). \quad (37)$$

To fully determine this solution, we must fix the constant $D_{\omega\ell}^I$. To do so, we compare the asymptotic solution obtained before (32) with the above solution at low frequencies (37). In a way, we are gluing the solution in the intermediate region with the boundary condition at infinity. To this end, we use the asymptotic form of the Legendre polynomial for large argument ($|z| \gg 1$),

$$P_\ell(z) \simeq \frac{(2\ell)!}{2^\ell (\ell!)^2} z^\ell, \quad (38)$$

in order to obtain the radial modes at this level of approximation,

$$\psi_{\omega\ell}(r) \simeq D_{\omega\ell}^I \frac{(2\ell)!}{2^{(\ell+1)} (\ell!)^2} \left(\frac{r/M}{1-q^2} \right)^{\ell+1}. \quad (39)$$

Expanding (32) around $\omega = 0$ or $\omega r \ll 1$, we arrive at the following asymptotic form

$$\begin{aligned} \psi_{\omega\ell} \simeq & A_{\omega\ell} [(-i)^{1+\ell} + i^{1+\ell} R_{\omega\ell}] \frac{2^\ell \ell!}{(2\ell+1)!} (\omega r)^{(\ell+1)} \\ & + A_{\omega\ell} i [(-i)^{1+\ell} - i^{1+\ell} R_{\omega\ell}] \frac{(2\ell)!}{2^\ell \ell!} (\omega r)^{-\ell}. \end{aligned} \quad (40)$$

Putting together (39) with (40), we arrive at the following coefficient

$$D_{\omega\ell}^I = A_{\omega\ell} (-i)^{(1+\ell)} [1 + (-1)^{(1+\ell)} R_{\omega\ell}] \times \frac{\ell! 3^{2\ell}}{(2\ell)! (2\ell+1)!} (\omega M)^{(\ell+1)} (1-q^2)^{(\ell+1)} \quad (41)$$

which leads to a reflection coefficient $R_{\omega\ell} = (-1)^{(1+\ell)} + \mathcal{O}(\omega)$ at low-frequency. As result of that, the radial modes are almost fully reflected by the effective potential (27). For $q = 0$ we return to the same result for the Schwarzschild metric [29]. Inserting (41) in (37) leads to the radial modes at low-frequency. With the latter solution at hand we can calculate the absorption cross-section within this limit, in fact, the cross-section will mostly depend on frequency of the incoming wave and the black hole parameters. Furthermore, close the black hole ($r \simeq 2M$) in the limit of low-frequency the scalar field can be written as

$$\psi_{\omega\ell} \simeq A_{\omega\ell} (-i)^{(1+\ell)} \frac{\ell! 2^{(\ell+2)}}{(2\ell+1)!} [\omega M \sqrt{1-q^2}]^{(\ell+1)}. \quad (42)$$

In order to compute the cross-section with the above solution (37)-(41) we must provide a general definition. As an incoming wave approaches a target the probability of an absorption process to happen is indicated by the absorption cross-section [23]. The absorption cross-section is defined as

$$\sigma = -\frac{\mathcal{F}}{J_i} \quad (43)$$

where \mathcal{F} stands for the total absorbed flow. The ingoing flux is calculated by integrating the radial current (22) through a closed sphere S_r ,

$$\mathcal{F} = \int_{S_r} J^r r^2 d\Omega. \quad (44)$$

The incident current associated to a plane-wave is given by $J^z = \omega |A_{\omega\ell}|^2$. Combining the incoming current with (44) along with $|R_{\omega\ell}|^2 + |T_{\omega\ell}|^2 = 1$ [23], we obtain that the partial absorption cross-section reads

$$\sigma_\ell = \frac{\pi}{\omega^2} (2\ell+1) |T_{\omega\ell}|^2. \quad (45)$$

Eq. (45) tells us how to compute the partial cross-section whether we are interesting in the low-frequency limit or for a different value of ω ; in fact, this result is independent of global constant $A_{\omega\ell}$. The above expression can also be used to compute σ_ℓ numerically and get the total cross-section by summing over the different ℓ -terms:

$$\sigma_{abs} = \sum_{\ell=0}^{\infty} \sigma_\ell. \quad (46)$$

Eq. (30) can be recast as $\psi_{\omega\ell} = A_{\omega\ell} T_{\omega\ell} (1 + \mathcal{O}(\omega))$. Comparing the latter expression with (42), we arrive at the transmission coefficient at low-frequency,

$$|T_{\omega\ell}| = \frac{\ell! 2^{(\ell+2)}}{(2\ell+1)!} [\omega M \sqrt{1-q^2}]^{(\ell+1)}. \quad (47)$$

Replacing (47) in (45) and keeping the lowest order in ω , which corresponds to $\ell = 0$, the absorption cross-section reduces to

$$\sigma = 16\pi M^2 (1-q^2), \quad (48)$$

for which it follows that is proportional to the area of the spherical horizon, $\sigma = 4\pi r_h^2 g(r_h)$, as we could expect. This result is consistent with the absorption cross-section for massless scalar field in the Schwarzschild geometry with $q = 0$ [23], [24].

B. Numerical results for absorption

In this section, we are going to present our main findings about the absorption cross-section obtained with the numerical implementation of the partial wave method described above for *arbitrary frequency*. To numerically recover the partial and total absorption cross-section over the interval $x \in (-\infty, \infty)$ we must impose at the horizon and at infinity the following boundary conditions

$$\psi_{\omega\ell} = \begin{cases} T_{\omega\ell} e^{-i\omega x}, & x \rightarrow -\infty \\ e^{-i\omega x} + R_{\omega\ell} e^{+i\omega x}, & x \rightarrow +\infty \end{cases} \quad (49)$$

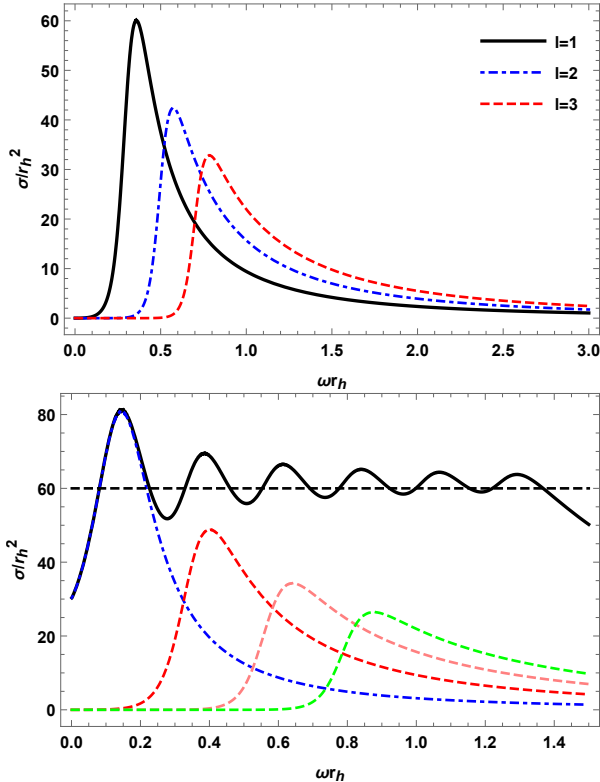


Figure 9: Absorption cross-section for a massless scalar on a dilatonic charged black hole with mass M and charge q in terms of $M\omega$. The dashed line is the geometric cross-section $\sigma \propto M^2$. The top panel shows different ℓ contributions and the lower panel depicts the total cross-section from $\ell = 0$ to $\ell = 5$.

and simultaneously solve the master equation (26) subject to the latter boundary condition (49). By taking the modulus of (49) and its derivative we can show that the transmission coefficient becomes

$$|T_{\omega\ell}|^2 = \left\{ \frac{1}{4} \left[|\eta_{\omega\ell}|^2 + \frac{1}{\omega^2} \left| \frac{d\eta_{\omega\ell}}{dx} \frac{dx}{dr} \right|_{x=x_\infty}^2 \right] + \frac{1}{2} \right\}^{-1} \quad (50)$$

where $\eta_{\omega\ell} = e^{-i\omega x} + R_{\omega\ell} e^{i\omega x}$. The transmission coefficient, and hence the absorption cross-section, is completely determined by (50), which is solved numerically as we stated before. Fig.(9) shows the absorption cross-section in terms of the decoupling parameter $M\omega$. For each value of ℓ the pattern of the cross-section has a main peak and then decays to zero. As result of that, the total cross-section ends up with a series of peaks and then vanishes for large $M\omega$. The $\ell = 0$ term is the main contribution for small values of $M\omega$ provided the other partial term are suppressed by the geometric-optic limit. Notice that each size of the peak is typically of order $\mathcal{O}(M\omega)^{-1}$ [24]. The reason for having a vanishing cross-section for large value of ℓ is easy to understand, greater the value of ℓ stronger the potential barrier becomes. Besides, Fig.(10) illustrates the comparison among to-

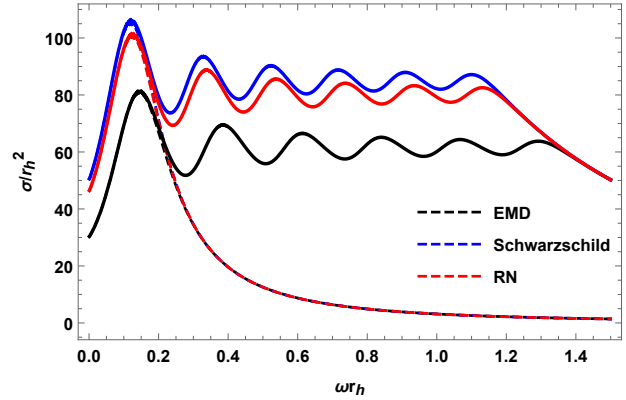


Figure 10: Total absorption cross-section for EMD, Schwarzschild, and RN black holes. The blue line is Schwarzschild, the red line is RN and the black line is EMD. The angular momentum varies from $\ell = 0$ to $\ell = 20$.

tal absorption cross-section for dilatonic, Schwarzschild, and RN black holes. It turns out that the amplitudes of the first peak differ a little bit, in the sense that RN and Schwarzschild have almost the same order of magnitudes, but dilatonic black hole exhibits considerably lower amplitude. In relation to Schwarzschild case, the peaks associated with the RN and EMD black holes are shifted to the right. As we stated before, all the profiles tends asymptotically to the same value.

C. Scattering cross-section

In this section, we are going to compute numerically the scattering cross-section for dilatonic black holes. To do so, let us begin by recalling how the differential cross-section is computed. The total wave function for a Schrödinger equation in a scattering problem with a central potential can be written as $\Phi_t = \Phi_0 + \Phi_s$, indicating the contribution of a free incoming wave Φ_0 along with the scattered wave, Φ_s [23]. For sake of simplicity, the ingoing wave has a wavenumber vector along the z -axis, $\Phi_0 \propto e^{i\omega z}$. The free wave term can be written in term of the spherical Bessel function and the Legendre polynomial as follows [23]:

$$e^{i\omega z} = \sum_{\ell=0}^{\infty} (2\ell+1) i^\ell j_\ell(\omega r) P_\ell(\cos\theta). \quad (51)$$

The spherical Bessel function in (51) includes an ingoing term and an outgoing spherical wave, so we must isolate the contribution which respect the boundary condition at infinity. Using the asymptotic expansion of $j_\ell(\omega r)$ at infinity [49]-[50], we are able to obtain the asymptotic form for the scattered wave as $\Phi_s = f_\omega(\theta) e^{i\omega r}/r$, where

the scattering amplitude is given by

$$f_\omega(\theta) = \frac{1}{2i\omega} \sum_{\ell=0}^{\infty} (2\ell+1) [e^{2i\delta_\ell(\omega)} - 1] P_\ell(\cos\theta), \quad (52)$$

and the complex-valued phase shift of the scattered wave is expressed in terms of reflection coefficient,

$$e^{2i\delta_\ell(\omega)} = e^{i(\ell+1)\pi} R_{\omega\ell}. \quad (53)$$

Using (52) the differential scattering cross-section reads $d\sigma_s/d\Omega = |f_\omega(\theta)|^2$, so the total scattering section is obtained by integrating over the solid angle [23], [29], [31], namely, the scattering cross-section is the resummation over the partial cross-section

$$\sigma^s = \sum_{\ell \geq 0} \sigma_\ell^s = \frac{\pi}{\omega^2} \sum_{\ell=0}^{\infty} (2\ell+1) |1 - e^{2i\delta_\ell(\omega)}|^2. \quad (54)$$

In other words, the main physical traits of the scattering cross-section is contained in the scattering amplitude (52) or equivalently in the phase shift (54). Putting together (46) and (54), we arrive at the total cross-section $\sigma_t = \frac{2\pi}{\omega^2} \sum_{\ell \geq 0} [1 - \Re(e^{2i\delta_\ell(\omega)})]$, which yields to the optical theorem, $\sigma_t = \frac{4\pi}{\omega} \Im f_\omega(0)$ [23]. In fact, we can determine the phase shift within the wave partial method (valid at intermediate scales, $\lambda \simeq r_h$) under certain conditions. Within the approximation of large angular momentum, we define the deflection angle as a function of a continuous ℓ variable [31], [51], and its relation with the phase shift is

$$\Theta(\ell) = 2 \frac{d}{d\ell} [\Re(\delta_\ell)]. \quad (55)$$

Considering that the impact parameter can be written as $b = (\ell + \frac{1}{2})/\omega$, and comparing (16) with (55), we pick up an expression for the derivative of the shift phase

$$\frac{d}{d\ell} [\Re(\delta_\ell)] = \frac{2M\omega}{(\ell + \frac{1}{2})} + \wp(q) \frac{(M\omega)^2}{2(\ell + \frac{1}{2})^2}, \quad (56)$$

where $\wp(q)$ is just a form factor which depends on dimensionless parameter q . Integrating (56) yields to an estimation of the phase shift within the geometric limit, where the first two orders read

$$\delta_\ell = 2M\omega \ln(\ell + \frac{1}{2}) - \frac{\wp(q)(M\omega)^2}{2(\ell + \frac{1}{2})} + \dots \quad (57)$$

The second possibility corresponds to the Born approximation [23], however, this approach is not applicable to the lowest order in (57) as was mentioned in [52]. Any other contribution in $\delta_\ell = \mathcal{O}[(M\omega)^n]$ with $n \geq 2$ can be obtained from the phase shift definition which involves the Born potential.

As we did previously for the absorption case, the scattering amplitude can be computed numerically by solving the equation (26) and extracting the reflection coefficient. We determined the differential scattering cross-section for different values of the decoupling parameter

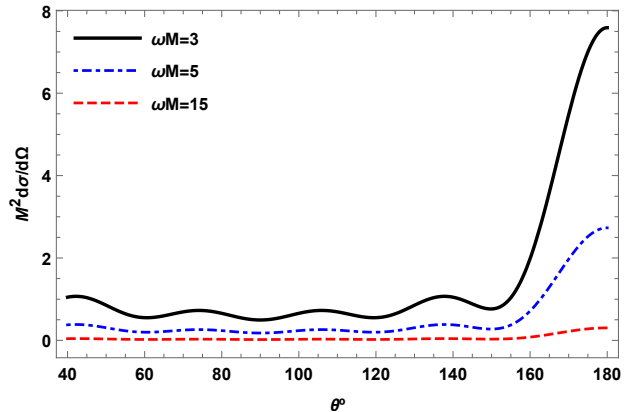


Figure 11: Scattering cross-sections for a massless scalar plane wave with angular frequency ω incident on a dilatonic black hole. Fixing q , the typical profile is shown for different values of $M\omega$.

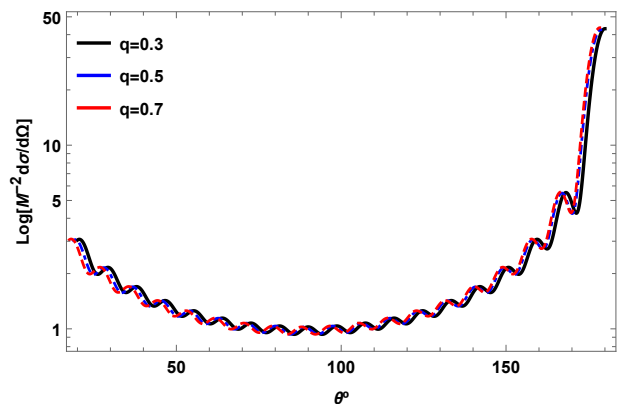


Figure 12: Logarithmic scattering cross-section as a function of the dispersion angle for different values of q with a fixed decoupling parameter, $M\omega = 3$.

$M\omega = 3$, $M\omega = 5$ and $M\omega = 15$ [see Fig.(11)] for a given value of q . The profile exhibits a series of oscillations whose amplitudes increase as the angle approach to 180° , signaling the relevance of the glory effect [29]. The typical pattern of the differential scattering cross-section, in logarithmic scale, is shown in Fig. (12) for different value of q with a fixed value of $M\omega$; increasing the value of q does not change the pattern significantly. For smaller angles, we obtain that the higher the q value is then lower the amplitude becomes, whereas the situation is reversed for larger angles.

Having performed all the above numerical analysis, we can go even further and compare the scattering cross-section with the corresponding curve obtained under the backward glory effect approximation for several values of q but with fixing decoupling parameter, $M\omega = 15$. Fig. (13) illustrates this point, for angle considerably smaller than $\theta = 180^\circ$ both curves do not agree, how-

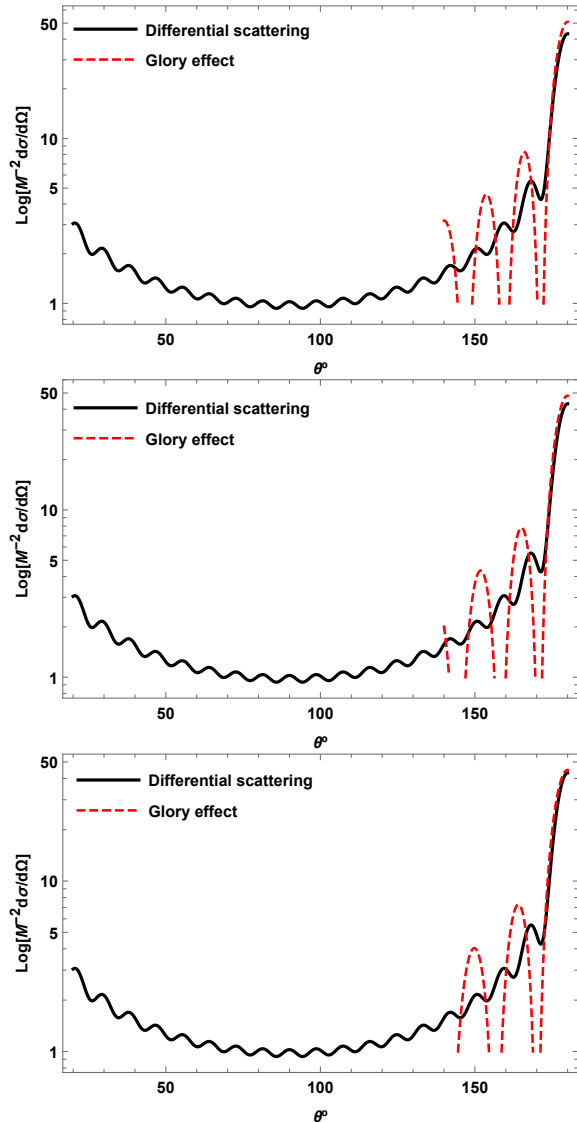


Figure 13: Differential scattering cross-sections as a function of the dispersion angle with $M\omega = 15$ in logarithmic scale.

ever, both findings seem to converge around $\theta = 180^\circ$. The latter fact does not seem to be affected by the value of q considered.

D. Absorption cross-section for high energies

So far we have been dealing with the analytic expression of the absorption cross-section in the limit of low-frequency, where the $\ell = 0$ mode represents the main contribution [23], [29], [31]. Of course, the general case is included in (45) and is achieved numerically by solving (26) with the proper boundary conditions, however, this procedure is time consuming as one ap-

proaches the regime of high frequencies. Nevertheless, it is still possible to obtain an analytic expression that captures the main traits of the absorption cross-section in the opposite part of the spectrum (high-energy). To do so, we are going to follow the method designed by Decanini and collaborators [39], [40], [41], [42] several years ago based on the complex angular momentum method. These authors showed that the main contributions for σ^a can be approximated by two terms of different nature. The optical contribution comes from the area associated with the photon sphere whereas the oscillatory part is modelled by the sinc function which involves the orbital frequency and the Lyapunov exponent of the null unstable geodesics [41]. Interestingly enough, the studies of determining an analytic formula in the high-frequencies limit goes back to the seminal paper of Sanchez, more than forty years ago [24]. However, the recent method developed by Decanini *et al.* is quite straightforward [41]. The starting point is to recall that the grebody factor is related with the transmission coefficient, $\Gamma_\ell(\omega) = |T_{\ell\omega}|^2$, and then to tackle the issue of computing the oscillatory part of absorption cross-section by using a complex angular method which includes isolating the Regge poles in the transmission coefficient with the help of the residues theorem, see [41] for further details. They proposed that the transmission coefficient which accounts for the decaying waves near the photon sphere (or the critical unstable null geodesic) are easily modelled by the following formula:

$$|T_{\omega\ell}|^2 = \frac{1}{1 + \exp\left[\frac{-2\pi(\omega^2 - V_0(\ell))}{\sqrt{-2V_0''(\ell)}}\right]}, \quad (58)$$

where the potential (27) and its second derivative in (58) near the maximum can be expanded as

$$V_0(\ell) = \frac{f_c}{r_c^2 g_c} (\ell + 1/2)^2 + \mathcal{O}_{\ell \rightarrow +\infty}(1),$$

$$V_0''(\ell) = -2 \left(\frac{\eta_c f_c}{r_c^2 g_c}\right)^2 (\ell + 1/2)^2 + \mathcal{O}_{\ell \rightarrow +\infty}(1), \quad (59)$$

and the critical radius r_c is obtained by making $V'(r_c) = 0$,

$$r_c = \frac{3 + q^2}{2} + \frac{\sqrt{9 - 10q^2 + q^4}}{2}, \quad (60)$$

In (59) the subindex c indicates quantities evaluated at the radius of the circular unstable geodesic. The maximum absorption is achieved for $\omega^2 \simeq V_0(\ell)$ [41],[32]. In the limit of high-frequency, the oscillatory part of the absorption cross-section is given by

$$\sigma_{\text{abs}}^{\text{osc}}(\omega) = -8\pi\sigma_{\text{geo}} \eta_c e^{-\pi\eta_c} \text{sinc}[2\pi b_c \omega], \quad (61)$$

in which the eikonal cross-section reads $\sigma_{\text{geo}} = \pi b_c^2$. The critical impact parameter is related to the critical radius through the expression $\omega^2 = f_c/r_c^2 g_c = b_c^{-2}$, and the

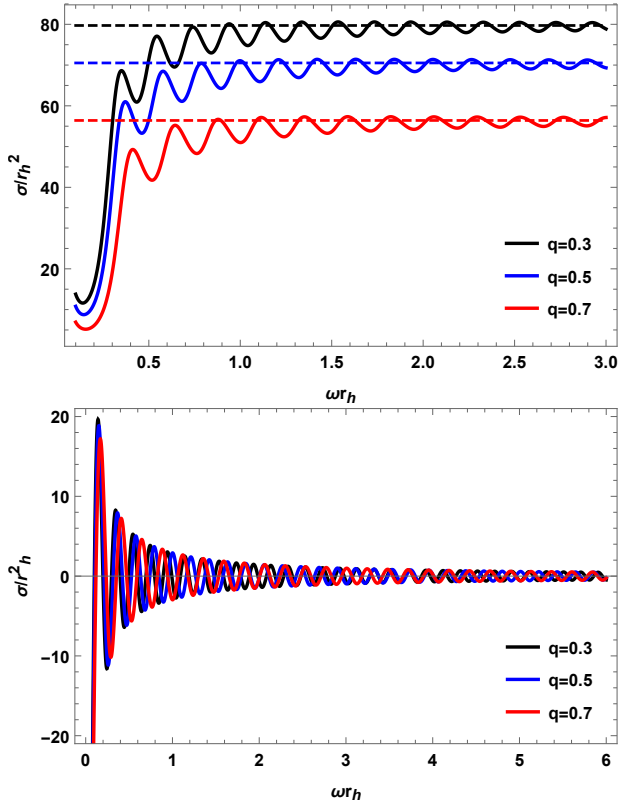


Figure 14: Top panel: Absorption cross-section for dilatonic black holes with different value of q ; the horizontal line indicates the geometric contribution to the cross-section. Low panel: Absorption cross-section for dilatonic black holes in the sinc approximation for different values of q .

parameter that accounts for the instabilities of the null circular orbits reads

$$\eta_c = \left[g_c(f_c - \frac{r_c^2}{2} f_c'') + f_c(2r_c g_c' + \frac{r_c^2}{2} g_c'') \right]^{1/2}. \quad (62)$$

The total high-frequency formula for the absorption cross-section is decomposed as $\sigma_{hf} = \sigma_{abs}^{osc} + \sigma_{geo}$ [40], [41]. In Fig.(14), we first show the absorption cross-section for the dilatonic black hole for several values of q , which was obtained numerically. Besides the oscillatory pattern, the cross-section decreases its amplitudes for small ωM as the parameter q takes larger values; a similar effect is observed in the case of the Reissner-Nordström black hole [30]. It can be seen that the contribution for each value of q is different in the sense that the curves are shifted to the right. Fig.(15) shows the comparison among the absorption cross-section for Schwarzschild, RN, and dilatonic black holes. The absorption cross-section for Schwarzschild black hole exhibits the largest amplitude whereas the dilatonic black holes has the smallest one, even smaller than the Reissner-Nordström black hole. This differ-

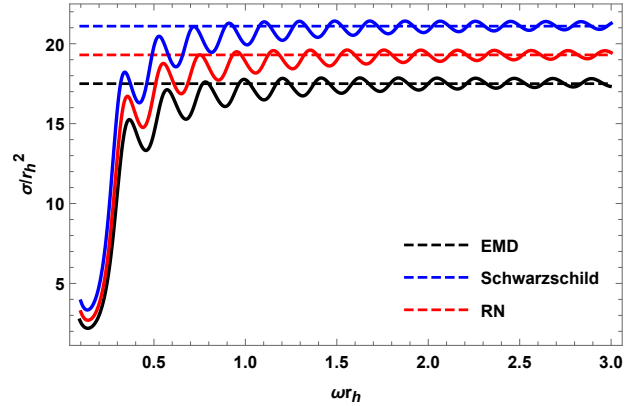


Figure 15: Comparison among the absorption cross-section of three types of black holes: Schwarzschild, RN, and dilatonic.

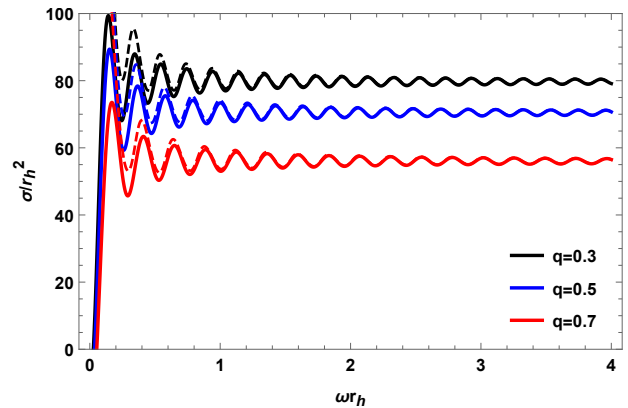


Figure 16: Total absorption cross-section for a massless scalar field in terms of ωM for three values of the charge-to-mass ratio, q . The continuous line is the numerical value and the dashed line represents the sinc approximation.

ence becomes relevant for large $M\omega$. At this point we must evaluate how good the sinc approximation is in relation with the full numerical absorption cross section. Fig. (16) displays both curves in terms of the decoupling parameter ωM for different values of q . The sinc approximation is in excellent agreement with the full numerical curve within the range $2M\omega \geq 1$, however, these curves can be distinguished for really small value of ωM , showing some kind of overestimation. Apparently, the larger the value of q is then the bigger is the difference between the full numerical curve and the sinc approximation. We continue our analysis by computing the difference between the numerical absorption cross-section and the high-frequency contribution within the sinc approximation. The idea is to examine the absolute estimator, $\Delta\sigma_{abs} = \sigma_{abs}^{num} - \sigma_{hf}$ [42]. It was found that in the case of Schwarzschild black hole there is a consider-

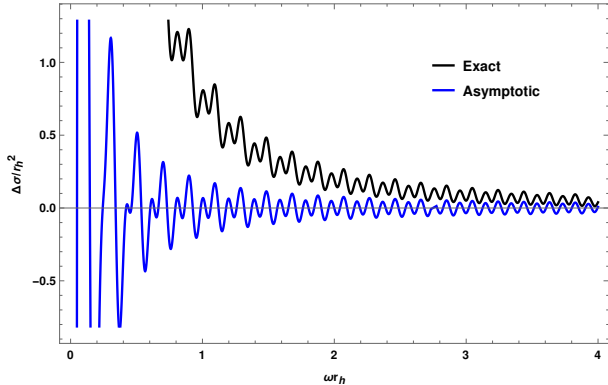


Figure 17: Difference between the numerical absorption cross-section and the high-frequency absorption cross-section. The black line represents $\Delta\sigma_{abs} = \sigma_{abs}^{num} - \sigma_{hf}$ (fine structure) and the blue line indicates the fluctuation $\Delta\sigma_{abs}^{hfine} = \sigma_{abs}^{h_o} - \sigma_{hf}$, where $\sigma_{abs}^{h_o}$ has higher order contributions and for that reason the supra-index h_o is added.

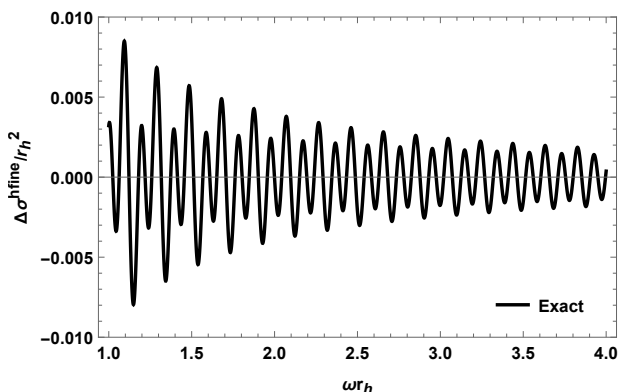


Figure 18: Hyperfine structure of the total absorption cross-section in terms of ωr_h in the case of dilatonic charged black hole.

ably small difference, typically below 5% as pointed out by Decanini *et al.* [42], [41]. In our case, the numerical simulation reveals that the fluctuation given by $\Delta\sigma_{abs}$ is really low, 0.3 order of magnitude, for $M\omega \gtrsim 2$ but this difference increases for $M\omega < 2$, reaching one order of magnitude [see Fig. (17)]. This fluctuation is known in the literature as the *fine structure* of the absorption cross-section [42], [41]. In fact, the analysis can be extended by considering higher terms in oscillatory part of the high-frequency approximation of the absorption cross-section [42]. The new corrections in the absorption cross-section read

$$\begin{aligned} \sigma_{abs}^{h_o} \simeq & \sigma_{geo} \left(1 - 8\pi \eta_c e^{-\pi\eta_c} \text{sinc}[2\pi b_c \omega] \right. \\ & \left. + 16\pi \eta_c e^{-2\pi\eta_c} \text{sinc}[4\pi b_c \omega] \right). \end{aligned} \quad (63)$$

Using (63) we can numerically estimate the absolute difference between $\sigma_{abs}^{h_o}$ and σ^{hf} . Fig. (17) indicates that these fluctuations are small for large $M\omega$. In a sense, this is indicating a numerical convergence provided we are comparing two consecutive terms. Additionally, we obtain the difference $\Delta\sigma_{abs}^{hfine} = \sigma_{abs}^{h_o} - \sigma^{hf} - \sigma_0$, being $\sigma_0 \propto \omega^{-2}$ a soft term derived in [42], [41]. This fluctuation is known as the hyperfine structure of the absorption cross-section because of the order of magnitude in the amplitude is around 0.001 whereas in the fine structure is around 0.01 [42]. The latter numerical analysis reveals a complex pattern in the high-energy absorption cross, different from the one related to the fine structure [see Fig.(18)].

V. CHARGED MASSIVE SCALAR FIELD

In this section, we are going to explore the case of a charged massive scalar field propagating on the dilatonic black hole background. In doing so, we will extend the previous analysis based on a neutral massless scalar field by focusing on the new features which are introduced by the mass of the field and its charge. The absorption cross-section due to the interaction of massive but neutral scalar field with a Reissner-Nordström black hole was explored in [32], where the cross-section was obtained at different frequency ranges (low, high, and intermediate). Some years later, the same authors revised their own analysis on the absorption of a massive scalar field by a Reissner-Nordström black hole, correcting some conclusions about the low-frequency limit [33]. In fact, Benone *et al.* used as a starting point a dimensionless parameter introduced by Jun and Park which helps to identify the role played by a massive scalar field in the absorption and emission spectra of Schwarzschild black hole [28]. The process of absorption of massive and charged scalar field by a Kerr-Newman black hole was reported in [53]. The absorption of massive wave of spin $s = 1/2$ around a small Schwarzschild black hole was explored by Doran *et al.* [54]. In the case of EMd gravity, the absorption cross-section associated with a massless scalar field was derived in [36], however, the analysis of a charged massive scalar field impinging upon a dilatonic charged black hole was not contemplated. Our main goal is to determine the absorption cross-section along with the scattering cross-section for a charged massive scalar field for a dilatonic black hole.

It is useful to introduce a dimensionless parameter, say v , which includes the field's mass and the incoming frequency/energy. Originally introduced by Jun and Park [28], this parameter reads

$$v = \sqrt{1 - \frac{m^2}{\omega^2}}, \quad (64)$$

and is well-defined ($0 < v \leq 1$) as long as $\omega > m$. To carry on, we consider the dynamic of charged massive

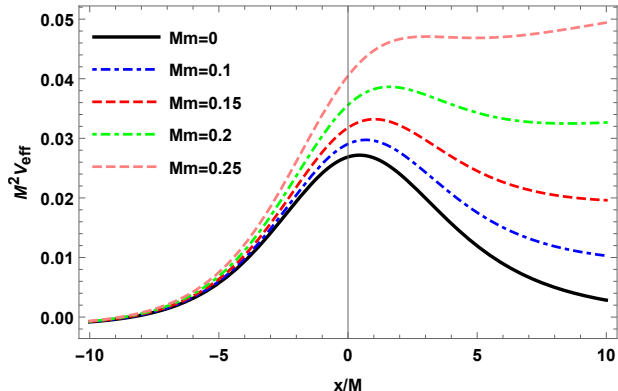


Figure 19: Effective potential in terms of tortoise coordinate for $\ell = 0$, $mk = 0.1$, $q = 0.4$, and different values of Mm .

scalar field near a dilatonic black hole (5), hence the master equation is given by a generalized Klein-Gordon equation

$$D^\mu D_\mu \Psi \equiv g^{\mu\nu} (\nabla_\mu - ieA_\mu) (\nabla_\nu - ieA_\nu) \Psi = m^2 \Psi. \quad (65)$$

Here e is the charge of the bosonic field, m is the mass of the scalar field, and ∇_μ stands for the covariant derivative in curved spacetime. The background electric potential is A_μ . As usual, we propose that the charged massive scalar field Ψ admits the usual decomposition (23). Replacing the latter ansatz in the generalized KG equation (65), we arrive at the Regge-Wheeler equation for the radial modes in the tortoise coordinate,

$$-\partial_{xx} \psi_{\omega\ell m} + \left(V - [\omega - eV_q]^2 \right) \psi_{\omega\ell m} = 0 \quad (66)$$

where the electric potential is $V_q \equiv A_t = \sqrt{2}Mq/r + k$ whereas the potential V reads

$$V(r) = f(r) \left[\frac{rf'(r)g'(r) + f(r)(2g'(r) + rg''(r))}{2rg(r)} + \frac{f'(r)}{r} - \frac{f(r)g'(r)^2}{4g(r)^2} + \frac{\ell(\ell+1)}{r^2g(r)} + m^2 \right]. \quad (67)$$

An issue regarding (66) is the selection of the effective potential provided we have V , V_q and a mixed term between V_q and ω . It is not clear which effective potential must be chosen, however, we are going to name as effective each term which does not the frequency:

$$V_{\text{eff}} = V - e^2 \left(\frac{\sqrt{2}qM}{r} + k \right)^2. \quad (68)$$

At this point we must summarize the main parameters of our geometry and the intrinsic parameters which characterizes the scalar field. The black hole presents originally three global charges M , Q , and $D = Q^2/2M$,

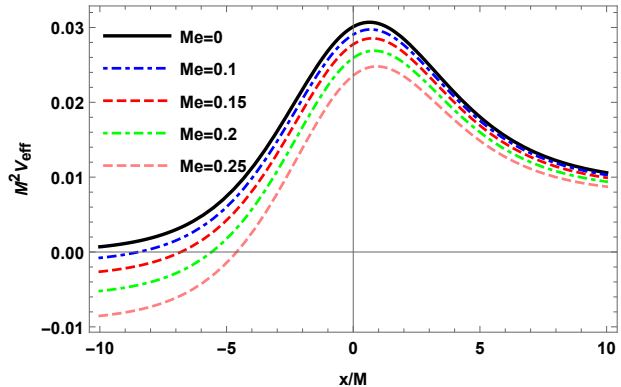


Figure 20: Effective potential in terms of tortoise coordinate for $\ell = 0$, $mk = 0.1$, $q = 0.4$ and some values of Me .

so it possible to define a dimensionless parameter $q^2 = D/M = Q^2/2M^2$ which assembles two of them, ending up with two parameters M and q . On the other hand, the scalar field has mass m , frequency ω , and charge e , so several combinations can be made in order to obtain dimensionless coupling, for instance, $M\omega$, Mm , and Mn with $n = \sqrt{m^2 - e^2k^2}$. The latter ones allow us to study different regimes which characterize the inner or far-field approximation but also how big/small the field mass is in relation with the black hole's mass. In addition to that, we introduce the concept of critical mass encoded in the Mn_c parameter following the Jung and Park prescription [28]. Indeed, the critical mass is defined in terms of the local maximum of the effective potential: $V(r \rightarrow \infty) = n^2$. In the far-field region we can expand the effective potential and consider only the corrections up to order $1/r^2$,

$$V_{\text{eff}} = (m^2 - e^2k^2) - \frac{2m^2M + 2M\sqrt{2}qe^2k}{r} + \frac{\ell(\ell+1) - 2M^2e^2q^2}{r^2}, \quad (69)$$

where the field's charge shifts the field mass. Another effect introduced by the field charge is that standard M -term includes a correction and the same happens for the standard angular momentum barrier (69). To better visualize how the shape of the effective potential changes with this Mn parameter, we add a plot of the effective potential in terms of x/M for different values of Mm or Me . Fig (19) shows up that the usual bell-shape of the effective potential is drastically modified as Mm is increased, that is, for higher values of Mm appears a local minimum besides the already existing local maximum. For values higher than the critical one, $Mm > Mn_c$, the unbound modes are absorbed for any value of ω . For instance, we obtain that the *effective* critical mass for $\ell = 0$ is $Mn_c = 0.195$, for $\ell = 1$ is $Mn_c = 0.338$, and for $\ell = 2$ reads $Mn_c = 0.517$. The relation be-

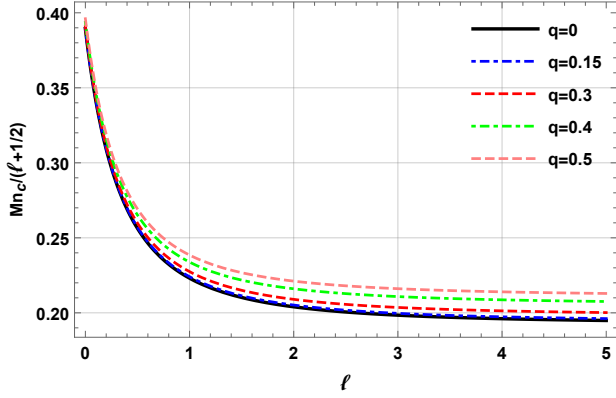


Figure 21: Critical mass coupling Mn_c as a function of multipole ℓ .

tween Mn_c and the angular momentum is displayed in Fig. (21), that is, for large value of ℓ the relation between both quantities becomes linear. We also check that the general shape of the potential does not change as Me increases, at least for large x/M , but V_{eff} becomes negative near the horizon provided the electric contribution seems to dominate over the gravitational terms [cf. (20)]. In order to solve the Regge-Wheeler equation (66) we must add some boundary conditions for the radial modes at the end of the interval. To do so, we notice that the effective potential vanishes at the horizon and goes to a constant m^2 at infinity. The boundary condition at the horizon must be an ingoing plane wave but at infinity there is a superposition of the outgoing wave plus an ingoing wave,

$$\psi_{\omega\ell m} = \begin{cases} T_{\omega\ell} e^{-i\xi x}, & x \rightarrow -\infty \\ e^{-i\rho x} + R_{\omega\ell} e^{i\rho x}, & x \rightarrow \infty, \end{cases} \quad (70)$$

where $\xi = \omega - eV_q(r_h)$ and $\rho = \sqrt{\bar{\omega}^2 - m^2}$. Using the definition of four-current vector (22) we infer the currents for the incoming, reflected, and transmitted waves,

$$J_x^T = \xi |T_{\omega\ell}|^2, \quad J_x^R = -\rho |R_{\omega\ell}|^2, \quad J_x^I = \rho. \quad (71)$$

From the conservation of four-current it follows the conservation of the flux associated with the spatial 3-current, $J_x^T = J_x^I + J_x^R$, which in terms of the amplitudes reads

$$|R_{\omega\ell}|^2 + \frac{\xi}{\rho} |T_{\omega\ell}|^2 = 1. \quad (72)$$

The extra-factor in front of the transmission coefficient (72) is signaling an interesting effect. To fully understand this aspect, we consider two different situations regarding the incoming wave near the black hole horizon. For $eV_q < 0$ the exponent of the incoming wave in (70) is positive. However, the exponent ξ could take negative value for $eV_q > 0$, and this wave turns into

an out-going wave which amplifies the already existing outgoing waves at infinity, showing up a superradiance phenomenon [43]. We will come back later to this topic in the final section and will explain in more detail, using a different point of view, the physics behind of it.

Using the same arguments mentioned in Sect. IVA for determining the partial absorption cross-section along with the change of $\omega \leftrightarrow \rho$, we obtain that the partial absorption cross-section reduces to $\sigma_\ell = (\pi/\rho^2)(2\ell + 1)(1 - |R_{\omega\ell}|^2)$. Replacing (72) in the latter expression, we arrive at the new formula for the partial absorption cross-section in terms of the transmission amplitude,

$$\sigma_\ell = \frac{\pi\xi}{\rho^3} (2\ell + 1) |T_{\omega\ell}|^2, \quad (73)$$

where ξ/ρ^3 factor accounts for the superradiance effect. In the case of a massless and chargeless scalar field $\rho^3 = \omega^3$ and $\xi = \omega$, and consequently, the extra-factor leads to the usual $\xi/\rho^3 = \omega^{-2}$ contribution. The total absorption cross-section is derived by summing over the partial contribution of each angular momentum, $\sigma_{\text{abs}} = \sum_\ell \sigma_\ell$.

A. Low-frequency regime

In this subsection, we tackle the computation of the absorption cross-section in the limit of low-frequency, $M\omega \ll 1$. In addition to that, we are supposing $mM \ll 1$ and $eq \ll 1$ to obtain analytical expressions [33]. This level of approximation is based on reasonable physical grounds, namely, the low-frequency condition implies that $mM \ll 1$ provided $m < \omega$. The second condition indicates that the electric field generated by the e -charge is really small in relation to the background electric field associated with the charged black hole. We are going to split the spatial region into three different zones, depending whether the wave is near the black hole (region I), in an intermediate region (region II) or far away from the compact object (region III). In fact, we also going to glue each local solution in order to assemble a global solution which satisfies the boundary condition stated before (70).

Let us begin by mentioning that the simplest case corresponds to the solution in region I provided the effective potential vanishes. For simplicity, we define $\phi_{\omega\ell m} = \psi_{\omega\ell m}/r\sqrt{g(r)}$ and write down the boundary condition listed in (70) as follows

$$\phi_{\omega\ell m}^I \approx T_{\omega\ell} (r - 2M)^{-2Mi\xi}. \quad (74)$$

In region II, we explicitly take the limit of low-frequency in the effective potential $M\omega \ll 1$ so we can neglect the ω term and the whole effective potential but keep the terms rising from the second derivative of $\phi_{\omega\ell m}$. In doing so, we employ the approximation $eq \ll 1$ to neglect

the background electric potential as well. The master equation reduces to

$$\frac{d^2 \phi_{\omega \ell m}^{II}}{dr^2} + \left(\frac{f'(r)}{f(r)} + \frac{g'(r)}{g(r)} + \frac{2}{r} \right) \frac{d\phi_{\omega \ell m}^{II}}{dr} = 0, \quad (75)$$

and its solution is

$$\phi_{\omega \ell m}^{II} \approx \frac{c_1}{\beta} \ln \left(\frac{r - 2M}{Mr - 2M^2 q^2} \right) + c_2, \quad (76)$$

where c_1 and c_2 are integration constants whereas $\beta = 2M^2(1 - q^2)$. To match the solution of region I (74) with the solution belonging to region II (76), we need to recast (74) in a different way,

$$\phi_{\omega \ell m}^I \approx T_{\omega \ell} [1 - 2Mi\xi \ln(r - 2M)]. \quad (77)$$

Near the horizon the second solution (76) reduces to

$$\phi_{\omega \ell m}^{II} \approx \frac{c_1}{\beta} \ln \left(\frac{r - 2M}{\beta} \right) + c_2. \quad (78)$$

It is straightforward to determine the integration constants by simply equating (76) and (78) in the superposition region,

$$c_1 = -2Mi\xi\beta T_{\omega \ell}, \quad (79)$$

$$c_2 = 1 - 2Mi\xi \ln \beta T_{\omega \ell}. \quad (80)$$

We carry on by looking at the shape of the master equation in far-field limit (region III). In this region, it is not possible to neglect the mass term neither the ω^2 term, however, the $2Me^2 q^2/r^2$ factor is neglected provided the condition $eq \ll 1$ holds, but the ek term cannot be discarded provided it will modify the effective frequency by generating a shift in frequency. Proceeding in the manner that we did before, (66) can be simplified as

$$\frac{d^2 r \phi_{\omega \ell m}^{III}}{dr^2} + \left(\bar{\omega}^2 - m^2 + \frac{\varpi}{r} - \frac{\ell(\ell+1)}{r^2} \right) r \phi_{\omega \ell m}^{III} = 0 \quad (81)$$

where $\varpi = [2Mm^2 - 4M\bar{\omega}^2 - 2M\sqrt{2qe\bar{\omega}}]$ and $\bar{\omega} = \omega - ek$. Eq. (81) resembles the well-known Coulomb wave equation in spherical coordinates [50]. Its solution can be recast in terms of the regular Coulomb function $F_l(\eta, \bar{\rho}r)$ and the irregular Coulomb function $G_l(\eta, \bar{\rho}r)$, respectively

$$\phi_{\omega \ell m}^{III} = a \frac{F_l(\eta, \bar{\rho}r)}{r} + b \frac{G_l(\eta, \bar{\rho}r)}{r}, \quad (82)$$

where the two parameters η and $\bar{\rho}$ are related in the following manner,

$$\eta = -\frac{M(2\bar{\omega}^2 - m^2 + \sqrt{2qe\bar{\omega}})}{\bar{\rho}}, \quad \bar{\rho} = \sqrt{\bar{\omega}^2 - m^2}. \quad (83)$$

Using the asymptotic expansion of the Coulomb functions [50] for large argument, the solution reduces to

$$\phi_{\omega \ell m}^{III} = Ae^{i\vartheta} + Be^{-i\vartheta}, \quad (84)$$

such that the phase is written in terms of the radial coordinate, angular momentum ℓ , and the two parameters that we introduced before plus an additional parameter δ_ℓ , namely, $\vartheta = \bar{\rho}r - \ell\pi/2 - \eta \ln(2\bar{\rho}r) + \delta_\ell$. Here, the new parameter $\delta_\ell = \arg\Gamma(\ell+1+i\eta)$ is the so-called Coulomb phase shift [50]. Taking into account (82) and (84) we can show how the integration constants are related to each other: $B = (-a + ib)/2i$ and $A = (a + ib)/2i$.

In order to match continuously the solution $\phi_{\omega \ell m}^{III}$ with the far-field solution $\phi_{\omega \ell m}^{II}$, we first have to determine a simple expression for the asymptotic expansion of (82). To do so, we work in the low-frequency ($M\bar{\omega} \ll 1$, $Mm \ll 1$, $Me \ll 1$) regime with zero angular momentum $\ell = 0$. The coulomb functions for $\ell = 0$ satisfy the next two identities: $iF_0(\eta, x) = \lambda x$ and $iG_0(\eta, x) = \frac{1}{\lambda}$. The λ parameter is written in terms of η , that is, $\lambda^2 = 2\pi\eta/[e^{2\pi\eta} - 1]$. With the help of the former identities, the general solution (82) admits a simple form,

$$\phi_{\omega \ell m}^{III} = a\lambda\bar{\rho} + \frac{d}{\lambda r}, \quad (85)$$

which can be glued smoothly in the far-field region with (78) after having expanded in series at infinity as

$$\phi_{\omega \ell m}^{II} = -\frac{c_1}{Mr} + c_2. \quad (86)$$

Combining (85) and (86), the integration constants in (85) are written in terms of the transmission amplitude,

$$a = \frac{1 - 2Mi\xi \ln \beta T_{\omega \ell}}{\lambda\bar{\rho}}, \quad (87)$$

$$d = 2i\xi\beta\lambda T_{\omega \ell}.$$

Replacing (87) in the definition of the coefficients A and B , we arrive a formal expression for the reflection coefficient,

$$|R_{\omega \ell}|^2 = \frac{|A|^2}{|B|^2} = \frac{|1 - 2Mi\xi \ln(\beta) - 2\xi\beta\lambda^2\bar{\rho}|^2}{|1 - 2Mi\xi \ln(\beta) + 2\xi\beta\lambda^2\bar{\rho}|^2}. \quad (88)$$

The connection with the absorption cross-section (73) is obtained by putting together (72) and (88). Indeed, the absorption cross-section with $\ell = 0$ in the low-frequency regime reads

$$\sigma_{abs} = \frac{\pi}{\bar{\rho}^2} \left[\frac{8\xi\beta\lambda^2\bar{\rho}}{(1 + 2\xi\beta\lambda^2\bar{\rho})^2 + 4M^2\xi^2 \ln^2 \beta} \right] \quad (89)$$

In general, (89) has a non-trivial behavior with the frequency and therefore we must look for an asymptotic expression that can be easy to compare with the numerical simulations. Bearing in mind that we are then considering an approximated formula for low-frequency only, it is valid to employ that $\lambda \approx 1$. Replacing the latter approximation in (89) and using that $v \gtrsim v_c = 2\pi Mm$ we obtain an analytic expression,

$$\sigma_{abs} \approx \frac{8\pi\beta\xi}{\bar{\rho}}, \quad (90)$$

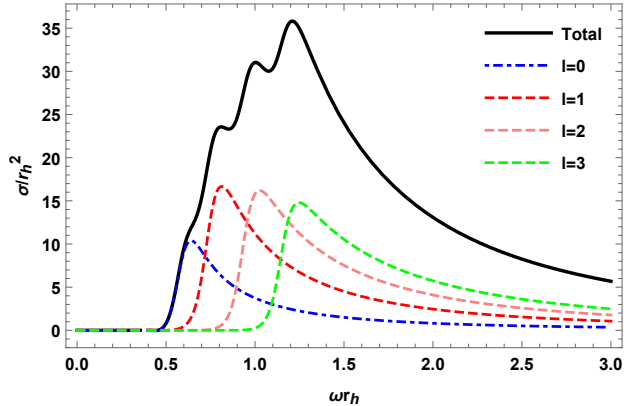


Figure 22: Partial and total absorption cross-sections in terms of ωr_h for a charged massive scalar field and a charged dilatonic black hole. Some parameters are fixed as $Me = 1.6$, $Mm = 0.4$ and $q = 0.4$ whereas the angular momentum ℓ varies. Due to the time consuming issue in computing σ_{abs}^{num} the resummation was performed using low value of ℓ_{max} .

which reduces to the Schwarzschild case, $\sigma_{abs} = 16\pi M^2/v$, for $q = 0$. In addition to the previous limit, we must explore another scenario where the v parameter is small but it could be near the critical velocity value, $v \lesssim v_c = 2\pi Mm$ [33]. If that is the case, the λ parameter can be calculated in the limit $\bar{\rho} \rightarrow 0$ again, but now, there are some corrections due to the fact the field has mass and charge,

$$\lambda^2 \approx \frac{2\pi M(m^2 + \sqrt{2}q em)}{\bar{\rho}}. \quad (91)$$

Replacing (91) in (90), the new absorption cross-section reads

$$\sigma_{abs} \approx 32\pi^2 M^3 (1 - q^2) (m^2 + \sqrt{2}q em) \frac{\xi}{\bar{\rho}^2}. \quad (92)$$

Eq. (92) agrees with the Schwarzschild case for $e = 0$, that is, $\sigma_{abs} \approx A^2(r_h)Mm/(2v^2)$ for $v < v_c$ [33]. In general, we are going to use $v = \bar{\rho}/\xi$ for plotting the absorption cross-section in terms of v provided this definition agrees with the case $e = 0$ employed before. Now, we are in position to present the exact/numerical results regarding the absorption cross-section. We begin by showing the numerical absorption cross-section for different values of angular momentum and its total resummation. Fig.(22) shows the partial absorption cross-section for $\ell = \{1, 2, 3\}$ and the total absorption cross-section for a dilatonic charged black hole in the case of a charged massive scalar field. The general pattern is a main peak for mildly frequency, $\omega r_h \simeq 1.2$, plus a series of oscillation of lower amplitudes for small frequency and then decays to zero for large ωr_h . The numerical analysis reveals that the partial cross-section for a given ℓ is much sensitive to the

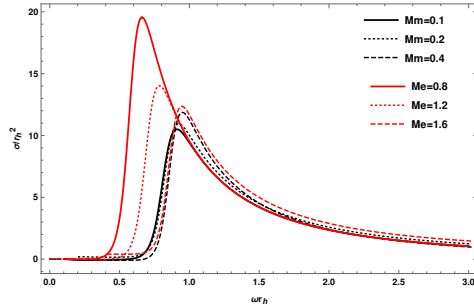


Figure 23: Partial absorption cross-section in terms of ωr_h for a charged dilatonic black holes and a massive charged scalar field. The red lines corresponds to different values of $Mm = \{0.1, 0.2, 0.4\}$ while the other parameter are fixed ($e = 1.6$, $\ell = 1$ and $q = 0.5$), whereas the black line is associated with the partial absorption cross-section for different values of $Me = \{0.8, 1.2, 1.6\}$ but fixing other parameters as follows, $Mm = 0.1$, $\ell = 1$ and $q = 0.5$.

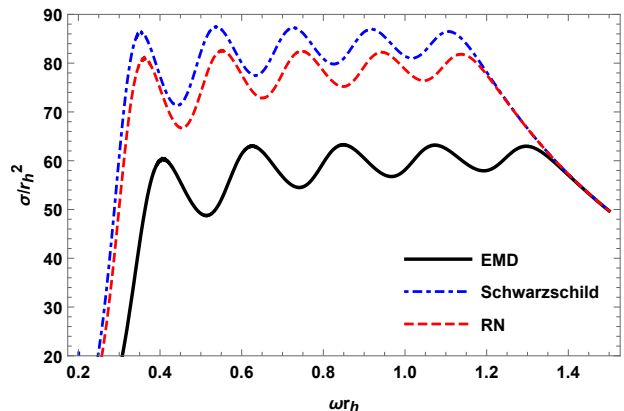


Figure 24: The total absorption cross-section for EMD, RN, and Schwarzschild black holes. The fixed parameters are $Me = 0.2$, $Mm = 0.2$, $q = 0.4$, $ek = 0.1$, and $\ell = 1$.

variation of Me than the variation of Mm as is shown in Fig. (23). Comparing the numerically-obtained total cross-section for the dilatonic black hole with the RN black hole, we obtain that the latter one has a much larger amplitude (similar to the Schwarzschild case) for $0.3 \leq \omega r_h \leq 1.3$, whereas the three numerical cross-sections converge to the same value for larger value of ωr_h [cf. Fig. (24)]. Another interesting point is to compare how good is the approximated absorption cross-section for low-frequency in relation with the full numerical solution [see Fig. (25)]. The relative error $\log \Delta\sigma_{abs}/\sigma^{num} = \log |\sigma^{num} - \sigma^{low}|/|\sigma^{num}|$ is really large at $v \simeq 0$ due to some numerical instabilities around that point, however, $\log \Delta\sigma_{abs}/\sigma^{num} \leq 1$ for $v \in (0, 0.4)$. It reaches its minimum value of 0.0042 at

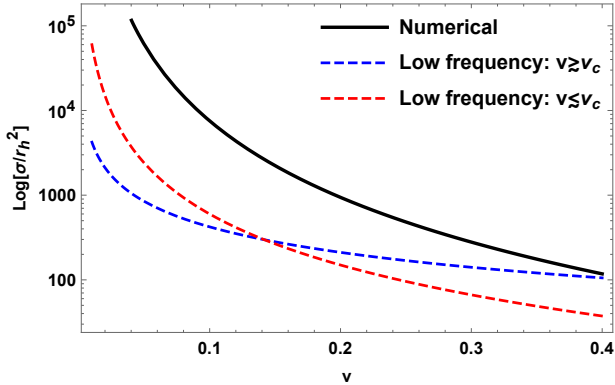


Figure 25: Comparison among the approximated absorption cross-section for low-frequency with $v < v_c = 0.138$, low-frequency with $v > v_c = 0.138$, and the full numerical absorption cross-section in logarithmic scale. The fixed parameters are $Mm = 0.022$, $Me = 0.001$, $k = 0$, $q = 0.4$ and $\ell = 0$. The black line corresponds to the numerical cross-section.

$v \simeq 0.42$ and then continuous to grow until $v = 0.8$ where its amplitude remains below the unity; therefore, this is a good approximation only on the interval $v \in (0.4, 0.8)$. In the opposite limit ($v < v_c$), we obtain that the approximated cross-section only described the problem qualitatively provided $\log[\Delta\sigma_{abs}/\sigma^{num}]$ is less than the unity on the interval $v \in (0.1, 0.8)$. From the previous analysis, we conclude that there is a transition in the cross-section at low-frequency around $v = 0.138$, as is seen in Fig. (25), and that both approximated cross-sections are good enough in each domain to describe the main behavior of the full numerical cross-section.

Before closing our analysis on the absorption cross-section, we would like to explore the physical consequences on the critical values obtained for v_c . We can proceed in three different manners. First, we consider the dark matter is accommodated as a chargeless scalar field with an ultralight mass $m_X \approx 10^{-22} \text{ eV}/c^2$ and with really low speed, $v_X \approx 4 \times 10^{-4}$ [56]¹. For a black hole such as Cyg X-1, recent measurements indicate a stellar mass of $M_{BH} = (21.2 \pm 2.2)M_\odot$ [57]. Then, the critical velocity becomes $v_c \simeq 10^{-11}$, a much smaller value than v_X , and for that reason we can use the distribution in the region $v \gg v_c$. In the case of black hole with intermediate masses $10 < M_{BH} < 10^5$ [58], the critical velocity varies over the interval $10^{-12} < v_c < 10^{-8}$, so it is clear once again that $v_X \gg v_c$. The

recent observation of a supermassive black hole called *IZw1* using the X-ray telescopes NuSTAR13 and XMM-Newton14 in the hard band of X-ray made possible the determination of its mass, $M_{BH} = (3.1 \pm 0.5)10^7 M_\odot$ [59]. Using the latter value, the critical velocity reads $v_c \simeq 2.3 \times 10^{-5}$, hence we must continue to use the region where $v \gg v_c$, or equivalently, the ultralight dark matter model is properly described by the $v_X \gg v_c$ phase. In order to break this tendency we must consider compact object supra-massive, for instance, the supermassive black hole located in the supergiant elliptical galaxy called Virgo A–Messier 87– has a mass $M_{BH} = (6.4 \pm 0.5)10^9 M_\odot$ [7]. Using the latter value, we obtain that the critical velocity $v_c = 5.3 \times 10^{-3}$, and therefore, it is appropriate to use the cross-section in the interval $v_X \ll v_c$. In the E4 supergiant elliptical galaxy called NGC 4889, a supermassive black hole was detected with a bigger mass, $M_{BH} = (2.1 \pm 1.6)10^{10} M_\odot$ [60], which leads to a critical velocity two order of magnitudes below v_X ².

Second, we could consider a different scenario where the dark matter particle is accommodated as a heavier particle with a millicharge; this possibility corresponds to a range of masses and charges given by $m_X \simeq 1 \text{ GeV}$ and $e\epsilon \leq 10^{-14}e(m_X/\text{GeV})$ [61]. A more recent rough analysis revealed that $q_X/e < 10^{-13\pm 1}(m_X c^2/\text{GeV})$ [62]. Other estimations based on the physics of the early universe place different constraints on the mass belonging to the MeV scale, $m_X \in [1, 80] \text{ MeV}$, and a charge $q_X/e < 10^{-6}$, respectively [63]. Either way, we are going to start by considering a conservative estimation on the millicharged dark matter mass, say $m_X = \text{GeV}$, and a low velocity $v_X = 10^{-3}/3$ [61]. For stellar black hole [57], the critical velocity is $v_c \simeq 1.6 \times 10^{20}$, for intermediate black hole with $M_{BH} = 10M_\odot$ [58] it leads to $v_c \simeq 7.6 \times 10^{19}$, and for a supermassive black hole [59] we arrive at $v_c \simeq 7.6 \times 10^{25}$, namely, in all the case considered, the millicharged dark matter is well-described by the supercritical phase with $v_c \gg v_X$. Notice that the bounds obtained in [63] lead to mildly lower values of v_c . The range of critical values of v_c is not considerably improved in more sophisticated frameworks, namely, taking into account primordial black holes with masses $0.2 < (M_{PBH}/M_\odot) < 5$ [64], the critical velocity continues lie on the interval $1.5 \times 10^{15} < v_X < 3.8 \times 10^{16}$. A third option is to employ our previous results on the critical velocity ($v_c = 0.138$) to determine what range of black hole masses is favored by the constraints on each dark matter model. As an example, we examine the ultralight chargeless dark matter scenario [56] and use the relation $m_X M_{BH} = 2.1 \times 10^{-2}$ along with $m_X \lesssim$

¹ Here we are considering that dark matter can be described by a massive scalar field [56], but also, it can be represented by a massive millicharged scalar field [61]

² Regarding the value of v_X we may say that represents the average velocity (rms) for a given dark matter particle distribution in different physical scales.

$10^{-22}/c^2$ and $M_{BH} = f_{BH}M_{\odot}$. It turns out that the favored range for black hole mass reads $f_{BH} \gtrsim 1.73 \times 10^{11}$, then the supramassive black hole located in the elliptical galaxy NGC 4889 is the closest compact object to satisfy this relation provided $M_{BH} = (2.1 \pm 1.6)10^{10}M_{\odot}$ [60].

B. high-frequency

In this subsection, the opposite part of the spectrum associated with the absorption cross-section in the high-frequency limit is contemplated. We begin by analytically obtaining an estimation of the cross-section. We restrict ourself for the sake of brevity to a massive but chargeless scalar field ($e = 0$). Our first task is to determine the critical impact parameter of the unstable geodesic provided within the eikonal approximation, the absorption cross-section reduces to $\sigma_{hf} = \pi b_c^2$. The geodesic equation for massive particle at the equatorial plane ($\theta = \pi/2$) with an initial energy which corresponds to a unbound orbit reduces to

$$\dot{r}^2 = E^2 - f(r) \left(m^2 + \frac{L^2}{r^2 g(r)} \right). \quad (93)$$

Here, $\dot{r} = dr/d\tau$ denotes the radial velocity in terms of the proper time, τ stands for the proper time, $E = \dot{t}$ refers to the conserved energy, and the conserved angular momentum reads $L = r^2 g(r) \dot{\phi}$. It is convenient to introduce the impact parameter in terms of L , E , and the dimensionless velocity $v = 1 - m^2/E^2$, namely, $b \equiv L/(Ev)$ [32]. Replacing the definition of b and v in (93), the radial velocity becomes,

$$\frac{\dot{r}^2}{L^2} = \frac{1}{b^2 v^2} - f(r) \left(\frac{1 - v^2}{b^2 v^2} + \frac{1}{r^2 g(r)} \right). \quad (94)$$

Geodesic curves with an impact parameter $b < b_c$ coming from the infinity will be absorbed by the dilatonic charged black hole but those geodesics with a bigger impact parameter, $b > b_c$, will continue to go back to infinity after having passed near the black hole. To proceed further, we find the critical impact parameter of the unstable orbits by imposing the condition $\dot{r}(r_c) = 0$, yielding

$$b_c = \frac{r_c g_c^{1/2}}{v f_c^{1/2}} \left[1 - (1 - v^2) f_c \right]^{1/2}, \quad (95)$$

where the sub-index c denotes evaluation at the critical radius of the unstable orbits, which by the way, can be found by demanding that $[d\dot{r}/dr](r_c) = 0$, its implicit expression reads

$$r_c^2 = \frac{g_c}{f_c b_c^2 v^2 \left(\frac{f_c}{g_c} \right)'} \left((1 - v^2) f_c' - \frac{2f_c}{r_c} [1 - (1 - v^2) f_c] \right). \quad (96)$$

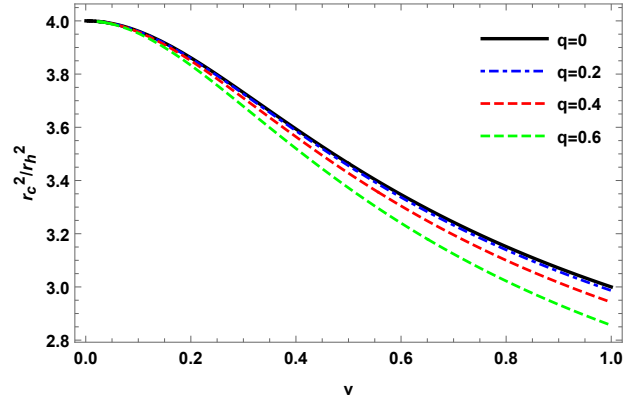


Figure 26: Critical radius of the unstable orbit in terms of the incident speed v for different values of charge-to-mass ratios q .

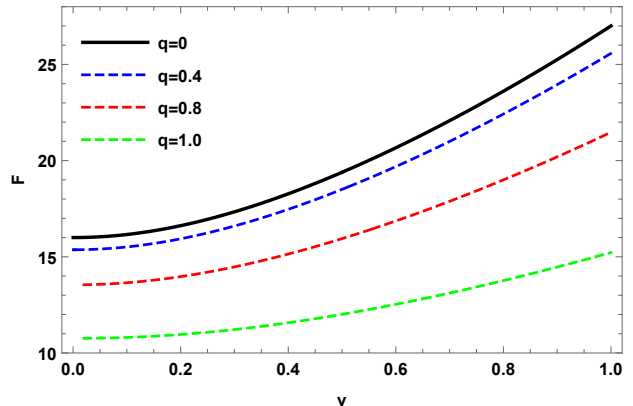


Figure 27: The form absorption function is depicted in terms of the incident speed v for various charge-to-mass ratios q .

In order to isolate the divergency of impact parameter as $v \rightarrow 0$, it is useful to define the form absorption function as $F(v, q) = v^2 b_c^2 / M^2$ [32] provided it remains finite in the former limit. The absorption cross-section then becomes

$$\sigma_{hf} = \frac{\pi F(v, q) M^2}{v^2}. \quad (97)$$

Once the critical radius is obtained numerically by solving (96) and the critical impact parameter is obtained from (95), we are able to determine the form absorption function. Fig. (26) illustrates the behavior of r_c in terms of v for different value of q , indicating that the lower the value of v is then the higher the critical radius becomes; besides, by increasing q we end up with a lower critical radius. A similar situation is obtained by exploring the typical profile of the form absorption function as a function of the incident velocity v for several values of charge-to-mass ratio [cf. 27].

To account for the full absorption cross-section, we

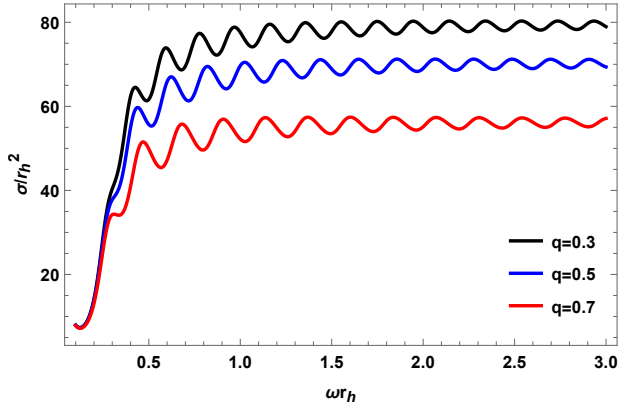


Figure 28: High-energy absorption cross-section in terms of ωr_h for different values of q for a dilatonic black hole. The other parameters are fixed at $Mm = 0.4$ and $e = 0$.

need to add the high-frequency contribution to the oscillatory part as we did before [41], [32]. Indeed, the oscillatory part is obtained by isolating the Regge poles [41] and it reads

$$\sigma_{\text{abs}}^{\text{osc}}(\omega) = -8\pi v b_c \Lambda e^{-\pi v b_c \Lambda} \sigma_{\text{geo}} \text{sinc}[2\pi v b_c \omega]. \quad (98)$$

Eq. (98) tells us that the oscillatory part involves the Lyapunov exponent, Λ , which is related with the unstable circular orbit in the sense that it can be employed as a measure of the average rate at which nearby trajectories converge or diverge in the phase space [55], it simply reads $\Lambda = [V''(r_c)/2\dot{t}^2(r_c)]^{1/2} = \eta_c/vb_c$. This exponent is evaluated at the peak in the potential barrier and numerical analysis shows that the greater q is then the lower the values of Λ are, or equivalently, the unstable circular orbits become more and more unstable as q takes lower values. The total absorption cross-section $\sigma_{\text{abs}} = \sigma_{\text{hf}} + \sigma_{\text{abs}}^{\text{osc}}$ is depicted in terms of ωr_h for some values of q [see Fig. (28)]. In fact, it is possible to show how the oscillatory part are mounted on the high-frequency absorption cross-section as is displayed in Fig. (29).

C. Numerical results for scattering

The main results for the scattering cross-section in the case of a charged massive scalar field are mentioned in the following. The new expressions can be derived by applying the same approach used in Sec. IVD, and in doing so, the frequency ω must be changed accordingly in order to account for the presence of the charged field, in a similar fashion as it was done in Sec.V. The boundary conditions used for running the numerical simulation are listed in (70) and the transmission coefficient which later on is replaced in (73) to get the partial scat-

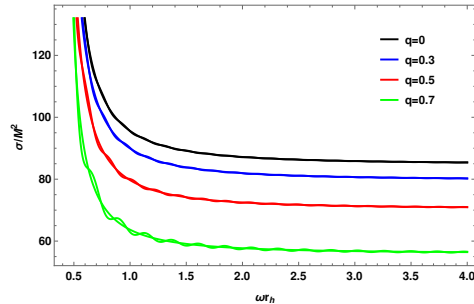


Figure 29: Oscillatory absorption cross-section along with the high-frequency cross-section in terms of ω/m for different values of q for a dilatonic black hole. The other parameters are fixed at $Mm = 0.4$ and $e = 0$.

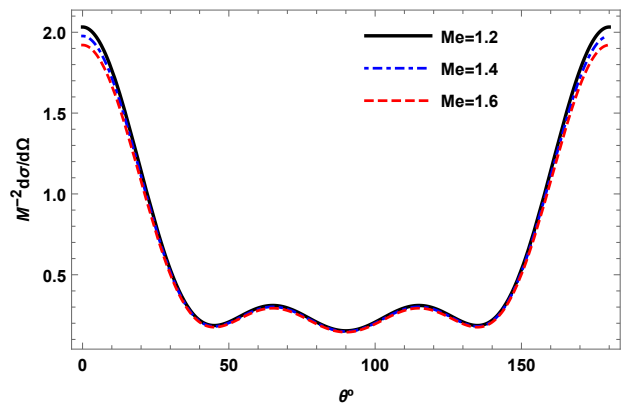


Figure 30: Differential scattering cross-section in terms of the angle for a dilatonic black hole with $Mm = 0.4$, $q = 0.5$, $M\omega = 3$ while varying Me .

tering cross-section can be recast as

$$|T_{\omega\ell}|^2 = \left\{ \frac{1}{4} \left[|\psi_{\omega\ell}|^2 + \frac{1}{\bar{\rho}^2} \left| \frac{d\psi_{\omega\ell}}{dx} \frac{dx}{dr} \right|_{x=x_\infty}^2 \right] + \frac{\xi}{2\bar{\rho}} \right\}^{-1}. \quad (99)$$

For $M\omega = 3$ we numerically obtained the differential scattering cross-section in terms of the angle for some values of Me [cf. Fig. (30)]. The general feature is a series of peaks with two maximums at the end of the interval. The variation of each height for different selections of Me is really small; in fact, the higher Me is then the lower values of $d\sigma_s/d\Omega$ are. The major distinction among these curves is close the critical angle 180° due to the backward glory effect, as is expected for massive s-waves. A similar situation is achieved by taking diverse values of Mm , as is shown in Fig. (31). However, higher amplitudes correspond to bigger values of the Mm parameter. Fig.(32) displays the differential scattering cross-section for Schwarzschild, RN, and dilatonic black hole. The highest amplitude over the angle interval corresponds to the dilatonic black hole, even close to the critical angle 180° , whereas the Schwarzschild and RN black holes have almost identical amplitudes.

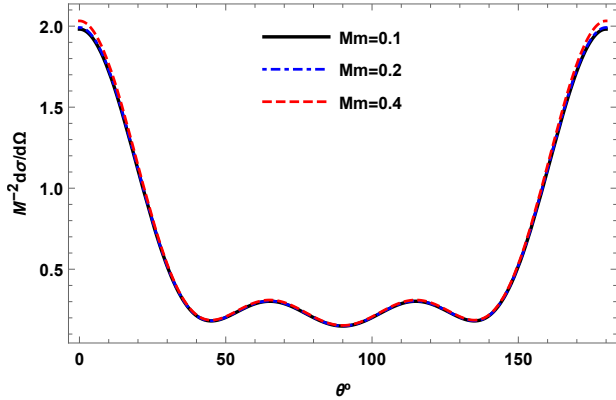


Figure 31: Differential scattering cross-section in terms of the angle for a dilatonic black hole with $Me = 1.2$, $q = 0.5$ and $M\omega = 3$ while varying Mm .

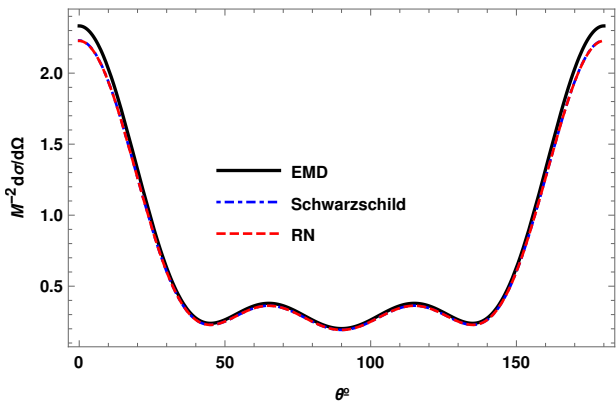


Figure 32: Differential scattering cross-section for Schwarzschild, RN, and dilatonic black holes with $Me = 0.8$, $q = 0.4$, $Mm = 0.1$, $M\omega = 3$. The selected maximum multipole was taken as $\ell_{max} = 3$ due to the time consuming effect of the numerical simulation.

VI. SUPERRADIANT SCATTERING

A. Numerical results

If a charged massive scalar field is scattered off by a charged black hole, under certain conditions, it is likely that the energy of the out-going wave becomes greater than the energy of the incoming wave. As a result of that, the outgoing modes at spatial infinity are amplified [43], [44]. The latter effect is known as the superradiant scattering [43]; a process by which the outgoing wave extracts energy from the black hole, in similar fashion as it happens in the Penrose's mechanism for extracting energy/angular momentum from a rotating black hole [3], [43]. If these modes are trapped on a well-potential such a process could lead to the so-called superradiant instability [43]. Having a system which exhibits a su-

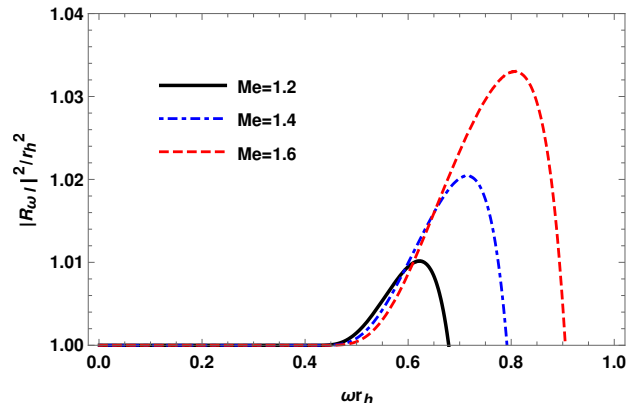


Figure 33: Reflection coefficient for a dilatonic black hole as a function of ωr_h while keeping fixed $Mm = 0.4$, $q = 0.8$, $\ell = 0$ but varying Me .

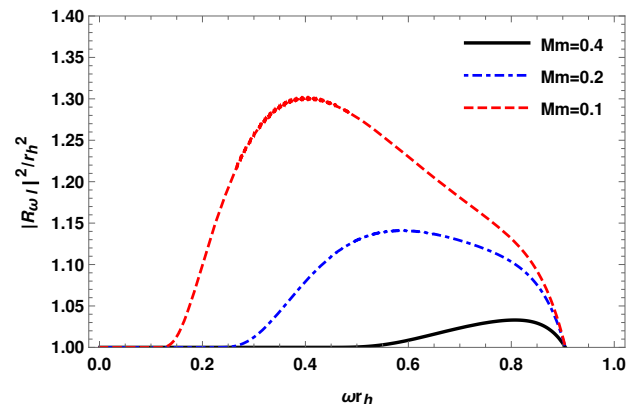


Figure 34: Reflection coefficient for a dilatonic black hole as a function of ωr_h while keeping fixed $Me = 1.6$, $q = 0.8$, $\ell = 0$ but varying Mm .

perradiance effect does not necessarily lead to a superradiant instability, additional conditions must be held. A simple way to visualize the superradiant scattering effect is by considering that the event horizon acts as a membrane that loses energy. Numerical studies of the superradiance effect were carried out for different kinds of black holes, namely, static black holes [44], stringy black holes [47], and Kerr-Newman black hole [53](see [43] more details). Numerically speaking, we can study the superradiance effect by solving (50) subject to the boundary conditions (30)-(34). We look under which conditions the reflection coefficient $|R_{\omega\ell}|^2 > 1$, signaling an amplification effect of the scattered waves. In Fig.(33), we illustrate the superradiant effect for a dilatonic charged black hole in terms of ωr_h by varying the Me parameter. These results indicate that higher values of Me lead to higher amplitudes in the $|R_{\omega\ell}|^2$ coefficient; however, we obtain the opposite effect by increasing the values of Mm as is shown in Fig. (34). We end up with this section by comparing the superradiance effect

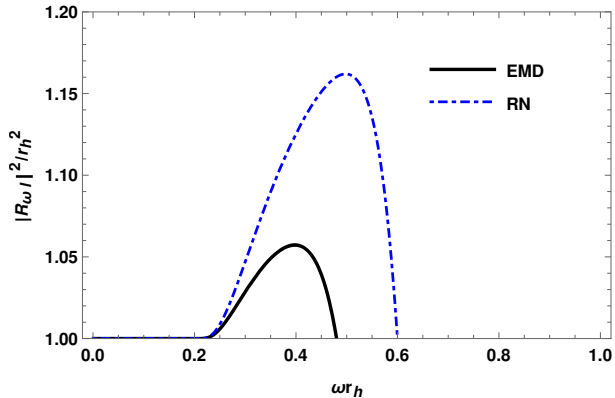


Figure 35: The reflection coefficient for RN black hole and dilatonic charged black hole are displayed for fixed $e = 1.2$, $q = 0.8$, and $\ell = 0$.

between two charged black holes, the RN black hole and the dilatonic black hole. It turns out the superradiance effect for dilatonic black hole is less powerful than the RN case, at least, for the case of a massive charged scalar field impinging upon a dilatonic black hole [cf. Fig. (35)]. A different perturbation could potentially enhance the superradiance effect for dilatonic black hole and it would be interesting to explore the case of electromagnetic perturbations. As can be seen, for mild decoupling parameter $\omega r_h \in (0.2, 0.6)$, the relative difference $||R_{EMd}^2 - |R_{RN}^2|/|R_{RN}^2|$ increases up to 0.08 near their peaks.

B. Superradiant instability

So far we have been dealing with the numerical analysis of the superradiance effect by which a charged massive scalar field extracts electrostatic energy from a charged dilatonic black hole. In order to better understand this mechanism, we are going to focus on a different aspect of it. We are going to explore what are the physical conditions which trigger the superradiant instability, and by doing so, we are going to determine the regions in the space parameter associated with it. Let us begin by explaining how the superradiant instability can take place [43] once again. The outgoing wave which gained energy from the charged black hole could admit a range in frequency by which the oscillatory modes change their nature, growing without limit over time. By creating a potential well in which these amplified modes remain trapped, a *black hole bomb* mechanism is ignited, destabilizing the black hole [65], [66]. There are several mechanisms which lead to a black hole bomb, including a reflecting mirror around a rotating black hole [67], a massive scalar field around a rotating black hole [68], a magnetic field

[69], [70], and massive scalar field around a Kerr black hole with a mirror-like boundary condition [71]. Regarding the case of nonrotating charged black hole impinging by a massive charged boson field, the possibility of creating a black bomb was explored by Hod in several seminal papers [72], [73], [74]. The main findings are that extremal and non-extremal Reissner-Nordström black holes do not meet the two necessary conditions for creating a charged black hole bomb, that is, the trapping potential outside the black hole and the growing trapped modes are not possible to achieve at the same time [72], [73], [74]. The outcome of this would seem to support the conjecture that charged black holes remain stable against charged massive boson perturbation. However, a year later the same author showed that for a charged black hole bomb exists of a lower bound on the charge-to-mass ratio such that the superradiant instability is triggered when the trapping modes are confined due to a mirror-like boundary condition [75]. There were also numerical evidences that RN black hole supporting the superradiant instability against massive charged perturbation of zero spin contained in a cavity; in fact, the final state of such configuration corresponds to a hairy black hole plus a boson condensate [76]. Besides, the case of charged RN impinged by a massive charged Dirac field was studied by Huang *et al.* [77], excluding the superradiance instability. For a massive charged boson field within a Kerr-Newman background, the superradiant instability would seem more favorable in comparison to a boson field around a Kerr black hole [78]. The inclusion of a negative cosmological constant for a Reissner-Nordström (RN-Ads) black hole and the superradiant instability was examined in [79]. The case of massive charged boson field which extracts energy from a stringy black hole was explored in [80], concluding that superradiant instability cannot be triggered provided the lack of trapping potential or growing modes. Subsequently, the stringy black hole was surrounded by a mirror which generates unstable modes for a massless charged boson field with large charge [81]. We are going to revisit [80]- [81] by considering a complementary scenario where a charged massive boson field lives within a charged dilatonic black hole, without separating between massive and non-massive case. Moreover, we are not going to set to zero the potential energy of the Abelian gauge field. In doing so, we will be able to explore the most general case of superradiant instability with charged massive field. Of course, our approach will follow the line of work devised by Hod [72], [73], [74], [75] and will benefit from the Li's methods as well [80], [81].

Before embark us in a full theoretical analysis of the superradiance effect and superradiant instability we would like to motivate even further our decision to continue studying charged (dilatonic) black holes. As is well-known charged black holes have been the center of debate of many appealing phenomena over the last fifty

years. For instance, the spontaneous loss of electric charge by a black hole and its connection with the polarization of vacuum was explored by Gibbons many years ago [82]. Rotating charged black holes (Kerr-Newman) was employed to determine diverse astrophysical constraints on the nature of minicharged dark matter and dark photons [83]. Some theoretical consistency based on the weak gravity conjecture for charged black holes like RN was also recently discussed [84]. The generation of gravitational wave due to charged matter colliding into a charged black hole was explored in [85]. Moreover, the linear stability of RN black hole was fully examined Refs. [86]-[87] in the last couple of years.

In order to determine whether a massive charged bosonic field Ψ on the stringy charged black hole background (5) can develop a superradiance instability or not, and subsequently, to explore for a confinement mechanism which traps the unstable modes, creating in this way a stringy charged black hole bomb, we begin by considering the modified KG equation (65) along with usual ansatz to separate variables, $\Psi = e^{-i\omega t} u_\omega Y_{\ell m}$. The master equation for the radial modes reads

$$\Delta \frac{d}{dr} \left(\Delta \frac{du_\omega}{dr} \right) + \left(\omega^2 \frac{\Delta^2}{f^2} - m^2 \frac{\Delta^2}{f} - \ell(\ell+1)\Delta \right) u_\omega + \left(e^2 A_t^2 + 2e\omega A_t \right) \frac{\Delta^2}{f^2} u_\omega = 0, \quad (100)$$

which can be written as

$$\Delta \frac{d}{dr} \left(\Delta \frac{d}{dr} \right) u_\omega + \mathcal{W} u_\omega = 0, \quad (101)$$

where $\Delta = r^2 f(r) g(r)$. We introduce a reparametrization $u_\omega = \hat{u}_\omega / r$ and a more convenient coordinate defined as $dy/dr = r^2/\Delta$ such that $-\infty < y < \infty$ [80], [81], provided is simpler to show that \hat{u}_ω satisfies the right boundary conditions at the end of the interval. In fact, (101) reduces to $\hat{u}_\omega'' + Z \hat{u}_\omega = 0$ with $Z = \mathcal{W}/r^4 - (\Delta/r^3) d(\Delta/r^2)/dr$. For the latter effective potential, we obtain that the asymptotic solutions are given by

$$\hat{u}_\omega = \begin{cases} e^{i\xi y} + A_\omega e^{-i\xi y}, & y \rightarrow -\infty \\ B_\omega e^{i\rho y}, & y \rightarrow \infty, \end{cases} \quad (102)$$

provided the effective potential approaches asymptotically to a constant $Z_{-\infty} = (1 - q^2)^2 \times [qe(\sqrt{2}/2)(\omega - ek)^2]^2$ as $y \rightarrow -\infty$, and in the opposite limit with $y \rightarrow +\infty$, the potential goes to a different constant $Z_{+\infty} = (\omega - ek)^2 - m^2$. In (102), we used $\xi = \omega - e(q\sqrt{2}/2 + k)$, $\rho = \sqrt{\bar{\omega}^2 - m^2}$ and $\bar{\omega}^2 > m^2$. For $\xi < 0$ we find that the outgoing wave extracts Coulomb-type energy from the charged black hole, amplifying the outgoing modes at infinity, signaling a superradiant scattering [72], [73], [74], [75], [80], [81]. Notice that our results agree with the work of Li and collaborators [80], [81], however, there are additional terms due to the zero

of electrostatic potential encoded in the k -term, and the fact that e and m are nonzeros at all times. To confirm the existence of superradiance, we explore the scattering problem for the modified KG with the boundary conditions (70). Using that the Wronskian is conserved, namely, $W(x \rightarrow -\infty) = W(x \rightarrow +\infty)$, we arrive at the following relation between the amplitudes,

$$|R_{\omega\ell}|^2 = 1 - \frac{(\omega - eA_t(r_h))}{\sqrt{\bar{\omega}^2 - m^2}} |T_{\omega\ell}|^2. \quad (103)$$

Eq.(103) tells us that the superradiance effect can take place if $\omega > ek + m$ and $\omega < eA_t(r_h)$, then the frequency range is $m + ek < \omega < eA_t(r_h)$. On the contrary, $\omega < ek - m$ and $\omega < eA_t(r_h)$, that is, $0 < \omega < \text{Min}\{eA_t(r_h), ek - m\}$.

We showed that the superradiant effect happens if a charged dilatonic black hole is perturbed by a massive charged boson field of zero spin. However, there is no evidence of superradiant instability. To evaluate this option we are going to analyze the effective potential outside de black hole horizon event, that is, we need to prove that the unstable modes are trapped in a potential well. We write $u_\omega = \psi_\omega/\sqrt{\Delta}$ and go back to the master equation (100) in the standard radial coordinates [80], [81],

$$-\frac{d^2\psi_\omega}{dr^2} + (\mathcal{U} - \omega^2)\psi_\omega = 0 \quad (104)$$

and the effective potential becomes

$$\mathcal{U} = \omega^2 - \frac{1}{4\Delta^2} (\Delta'^2 - 2\Delta\Delta'' + 4\mathcal{W}). \quad (105)$$

At this point we need to determine whether the effective potential (105) has a local minimum outside the black hole in order to enclose the unstable modes, which may induce the superradiant instability [80], [81]. Consequently, we compute the first derivative of the effective potential in terms of the $\varrho = r - 2Mq^2$ variable,

$$\mathcal{U}'(\varrho) = \frac{\varrho}{\Delta^3} (a\varrho^3 + b\varrho^2 + c\varrho + d), \quad (106)$$

where the coefficients are given by

$$a = 2M \left(2\omega[(\omega - ek) - eq\sqrt{2}] - 2m^2 \right), \quad (107)$$

$$b = 2M^2 \left(2(\omega - ek) - eq\sqrt{2} \right) \left[2(\omega - ek)q^2 - eq\sqrt{2} \right] + 4M^2 m^2 (1 - q^2) - 2\ell(\ell + 1), \quad (108)$$

$$c = 6\ell(\ell + 1)M (1 - q^2), \quad (109)$$

$$d = -2M\ell(\ell + 1) (1 - q^2)^2. \quad (110)$$

Eq. (106) has in principle four zeros denoted by $\{\varrho_0, \varrho_1, \varrho_2, \varrho_3\}$, one of them corresponds to the trivial root $\varrho_0 = 0$. In general, the zeros of a polynomial of

order three are related by the following expressions

$$\varrho_1 + \varrho_2 + \varrho_3 = \frac{b}{a}, \quad (111)$$

$$\varrho_1 \varrho_2 + \varrho_1 \varrho_3 + \varrho_2 \varrho_3 = \frac{c}{a}, \quad (112)$$

$$\varrho_1 \varrho_2 \varrho_3 = -\frac{d}{a}. \quad (113)$$

Using the critical frequency such that the superradiant effect takes place, $0 < \omega < \text{Min}\{eA_t(r_h), ek - m\}$, we arrive at $a < 0$. Looking at the asymptotic behavior of the potential and its derivative we obtain that

$$\begin{aligned} V'(r \rightarrow \infty) &\rightarrow 0^-, & V(r \rightarrow 2M) &\rightarrow -\infty, \\ V(r \rightarrow q^2 r_h) &\rightarrow -\infty. \end{aligned} \quad (114)$$

Eq. (114) is telling us that the effective potential vanishes at infinity and blows up near the horizon, and inside the event horizon the effective potential also diverges as $r \rightarrow q^2 r_h$ provided $0 < q < 1$ for a dilatonic black hole. Putting all together, we can conclude that the effective potential has a local maximum in the region outside the event horizon, and another over the interval $q^2 r_h < r < 2M$. Moreover, using the definition of the parameters (107) along with (111), it is easy to show that these two roots satisfy order relation $\varrho_1 > \varrho_2 > 0$. As long as the inequality $0 < q < 1$ holds, we have that $c > 0$ and $d < 0$, which together with the order relation $\varrho_1 > \varrho_2 > 0$ and (111), imply that the third zero must be negative, $\varrho_3 < 0$. Hence, there is not local minimum in the interval of interest, only two peaks. In summary, it is not possible simultaneously to have growing unstable modes and a well potential outside the horizon to enclose these modes, and therefore, the dilatonic charged black hole cannot be used to build a charged black hole bomb, at least taking into account the previous boundary conditions (102). Our next step is to explore a different kind of mechanism that may trigger the instability.

As we mentioned earlier there are several mechanism which may induce a superradiant instability [68], [69]. One of the most used in the literature corresponds to a mirror-like boundary condition [71], [75], [81]. In another words, we place a reflecting mirror for $r > r_h$ at the location $r = r_m$ demanding that none part of the scattered wave could be transmitted through it, $\psi_\omega(r = r_m) = 0$. A similar argument was used by Hod [75] and Li [81], independently. The backreaction effect due to the growing/unstable modes trapped in the potential well could potentially subvert the black hole itself.

Our next step is to consider the Schrödinger equation (66) along with the total effective potential $V_{\text{total}} = V - [\omega - eV_q]^2$, where V is given in (67). For practical reasons, it makes sense to define $V = f\mathcal{H}/r^2$ [75]. Let us begin by studying the local behavior of $\psi_{\omega\ell m}$ near the horizon, namely, we wish to determine whether $\psi_{\omega\ell m}$ has a maximum or minimum outside the horizon. To do

so, we introduce a new variable $\mathfrak{Z} = (r/r_h) - 1 \in (0, \infty)$. Imposing the superradiance condition encoded in (103), that is $\omega \ll [eq\sqrt{2}/2 + ek]$, we get rid of the terms which depend on the frequency in V_{total} , so we ended up with a potential proportional to the \mathcal{H} -term:

$$V_{\text{total}} = \frac{\mathcal{H}(r_h)\mathfrak{Z}}{r_h^2} + \mathcal{O}(\mathfrak{Z}^2), \quad (115)$$

where

$$\mathcal{H}(r_h) = 1 + m^2 r_h^2 + \frac{\ell(\ell+1)}{(1-q^2)} + \frac{q^2}{2(1-q^2)}. \quad (116)$$

First, we note that $\mathcal{H}(r_h)$ is positive defined provided $0 < q < 1$ for a dilatonic black hole. As a consequence of this, V_{total} is also positive near the event horizon. Now we replace (115) in the Schrödinger equation (66), yielding to the differential equation in terms of \mathfrak{Z} -variable [50],

$$\left(\mathfrak{Z}^2 \frac{d^2}{d\mathfrak{Z}^2} + 3\frac{d}{d\mathfrak{Z}} - \mathcal{H}(r_h)\mathfrak{Z}\right)\psi_{\omega\ell m} = 0, \quad (117)$$

which has as a general solution a linear combination of the modified Bessel function of order zero ($\nu = 0$),

$$\psi_{\omega\ell m} = c_1 I_0[\sqrt{2\mathcal{H}(r_h)\mathfrak{Z}}] + c_2 K_0[\sqrt{2\mathcal{H}(r_h)\mathfrak{Z}}]. \quad (118)$$

In order to keep the solution regular as $\mathfrak{Z} \rightarrow 0$, the coefficient c_2 must vanish. The solution $\psi_{\omega\ell m}$ is then a positive and convex function close to the horizon. To carry on, we need to investigate whether is possible to force a reflecting mirror-like boundary condition at r_m . In other words, we must prove that that the function $\psi_{\omega\ell m}$ has at least a maximum located at r_{max} such that $r_h < r_{\text{max}} < r_m$. This is equivalent to show that $\partial_{xx}\psi_{\omega\ell m}(r_{\text{max}}) = V_{\text{total}}(r_{\text{max}}) < 0$ [75]. Taking into account the total effective potential evaluated at r_{max} and replacing the value of the critical frequency, $\omega_c = e(q\sqrt{2}/2 + k)$, it follows that the total potential becomes

$$V_{\text{total}} = \left(\frac{r_{\text{max}} - r_h}{r_{\text{max}}}\right) \frac{\mathcal{H}(r_{\text{max}})}{r_{\text{max}}^2} - \frac{e^2 q^2}{2} \left(\frac{r_{\text{max}} - r_h}{r_{\text{max}}}\right)^2 \quad (119)$$

which can be translated in the following inequality,

$$\frac{eq}{\sqrt{2}} > \sqrt{\frac{r_{\text{max}}}{(r_{\text{max}} - r_h)} \frac{\mathcal{H}(r_{\text{max}})}{r_{\text{max}}^2}}. \quad (120)$$

However, we can improve the latter lower bound (120) provided the following condition $r_{\text{max}} < r_m$ holds. Indeed, we may employ the former inequality to change the constraints on r_{max} by one inequality which involves r_m ,

$$\frac{r_{\text{max}}}{(r_{\text{max}} - r_h)} > \frac{r_m}{(r_m - r_h)}, \quad \frac{\ell(\ell+1)}{r_{\text{max}}^2} > \frac{\ell(\ell+1)}{r_m^2} \quad (121)$$

Replacing (121) in (120), we arrive at an inequality in terms of eq and the position where the reflecting mirror is located, r_m ,

$$\frac{eq}{\sqrt{2}} > \sqrt{\frac{r_m}{r_m - r_h} \frac{\mathcal{H}(r_m)}{r_m^2}}. \quad (122)$$

In this way, we obtained a lower bound for eq such that the unstable modes remain trapped in a well potential for $\mathcal{H}(r_m) > 0$, indicating that the perfect mirror condition is a suitable mechanism for the creation of a charged black hole bomb as happens in the RN case [75]. Nevertheless, we must verify that the \mathcal{H} function is always positive defined outside the horizon. To show this numerically, it is useful to introduce some new variables called $0 < s = r_h/r_m < 1$, $0 < q < 1$, and $\bar{m} = 2Mm > 0$. Then, Eq. (122) can be recast as follows,

$$\frac{e}{m} > \sqrt{\frac{2s^2}{(1-s)} \frac{\mathcal{H}}{q^2 \bar{m}^2}}, \quad (123)$$

where the \mathcal{H} function depends only on dimensionless variables/parameters,

$$\mathcal{H} = s + \frac{\ell(\ell+1)}{(1-q^2s)} + \frac{s^2q^2}{1-sq^2} - \frac{s^2q^2(1-s)}{4(1-sq^2)} + \frac{\bar{m}^2}{s^2}. \quad (124)$$

Eq. (124) indicates that the \mathcal{H} function remains positive on the interval of interest. For instance, we can check this point by taking $\ell = 1$ and small scalar field mass, $\bar{m} = 0.6$, while plotting this function as the other variables run on the following intervals, $0 < s < 1$ and $0 < q < 1$. Also, we consider the case with $\ell = 1$ and large scalar field mass, $\bar{m} = 1.6$. In all the cases explored, we obtain that (123) satisfies the well-known lower bound $e/m \gtrsim 1$, in agreement with the RN case [75] and the numerical simulation reported in [76]. Even though these charged black holes are not found in Nature, they represent a nice toy model for helping us understand better the theoretical side of them, enlarging our views on black holes in extended theories of gravity ³.

VII. CONCLUSIONS

In this paper we have given an overview of the process of scattering and absorption of a massless scalar

field impinging on a charged dilatonic black hole within the framework of EMd gravity. While some of the results of Sec. III appear elsewhere, we motivated these results by confronting the analytical formulae with several numerical simulations. We obtained the differential cross-section in three different ways and compared with the one associated to the backward glory effect along with the semi-analytic estimation of the glory effect based on the logarithmic approximation, which seems to differ by 1% from the standard estimation of the glory effect. Near the critical angle, $\theta_c = \pi$, we found that the larger the charge-to-mass ratio q is then the smaller the amplitude of the differential cross-section becomes. In fact, the dilatonic charged black hole has smaller amplitude, near the critical angle, than the Reissner-Nordström case. Using the partial wave method for massless scalar field we numerically integrated the Schrödinger-like equation to reconstruct the partial and total absorption cross-sections in terms of the decoupling parameter $M\omega$. For instance, we showed that the total absorption cross-section has smaller amplitudes than Reissner-Nordström for mild frequency $M\omega \in (0.4, 1.2)$. We carried on by considering the absorption cross-section in the limit of high-frequency and discovered the existence of two different kinds of complex behaviors, also known as the fine structure and the hyperfine structure. The reason for selecting those names is based on the order of magnitude of their amplitudes in terms of ωr_h . We have validated these results by estimating the relative errors among the numerical solution and the approximated absorption cross-sections.

We have investigated also a massive charged bosonic field impinging on a dilatonic charged black hole. In this case, we have shown that in the limit of low-frequency the absorption cross-section can be derived by using a matching method to construct a global solution on the interval of interest $r \in (r_h, \infty)$, and by doing so, we showed the existence of two phases which are separated by a critical velocity parameter, v_c ; this parameter depends on the mass of the compact object and the mass of the scalar field. We have confirmed our previous analysis by performing again a numerical simulation of the total absorption cross-section for any frequency. For completeness, we have provided a full comparison of our numerical value of v_c and the typical velocity of dark matter in different scenarios, including black hole from stellar masses to supermassive black holes. In addition to that, we obtained the differential scattering cross-section for different values of field masses and charges, concluding that light but charged scalar field enhanced the differential scattering cross-section. We have determined numerically the reflection coefficient associated with the scattered waves. We found that there is a superradiant phenomenon because the squared of the reflection coefficient takes values larger than the unity for different values of mass' field (or the

³ An important fact in relation to the superradiance/superradiant instability for charged dilatonic black holes is that the reflection amplitude is lower than the Reissner-Nordström case. It would seem that the addition of a new degree of freedom does not necessarily help to enhance the superradiance effect. One way to understand this point is by noticing that both theories are not equivalent. Starting from $\phi = \phi_0 = cte$ in the EMd theory, we obtain that $F^2 = 0$ which can be satisfied by $F_{\mu\nu} = 0$, leading to $R_{\mu\nu} = 0$.

charge's field). We have verified that the superradiance scattering is enhanced by smaller values of scalar field mass but larger values of the scalar field charge. In the case of moderately frequency, we have found that the superradiant effect is lessen in relation with Reissner-Nordström case. To better understand the role played by these unstable modes, we have examined the mechanism that lead to a superradiant instability provided the former ones do not necessarily implies the existence of the latter one. The success of the superradiant instability lies on whether a potential well can be formed in the region outside the event horizon to enclose the growing modes. The mechanism that helps to come to fruition this possibility is known as the reflecting-mirror boundary condition. Further, we derived an analytical formula (lower bound) which determines the minimal value of the charge's field eq which may trigger the superradiant instability. A point that should be adressed in the near future is a fully nonlinear numerical simulation of the complete equation of motions to reply a simple question: What is the final state of the system composed of charged massive scalar field plus a dilatonic black hole? Recent nonlinear simulations seem to indicate that the final state could be a hairy black hole along with a condense scalar field provided the unstable modes are not allowed to leave the trapping potential. These findings would indicate that is possible to extract only a fraction of total charge of the black hole.

ACKNOWLEDGMENTS

M.G.R. is partially supported by Fundação de Amparo à Pesquisa e Inovação Espírito Santo (FAPES, Brazil) grant under the PPGCosmo Fellowship Programme. E.V.L.M is supported by Coordenação de Aperfeiçoamento de Pessoal de Nível Superior(CAPES, Brazil). J.C.F. is supported by Conselho Nacional de Desenvolvimento Científico e Tecnológico (CNPq, Brazil) and FAPES.

Appendix A: Penrose diagram

Given the metric associated with a static dilatonic black hole

$$ds^2 = -f(r)dt^2 + f^{-1}(r)dr^2 + r^2g(r)d\Omega^2, \quad (\text{A1})$$

with $-\infty < t < \infty$ and $2M < r < \infty$, we like to find its corresponding the Penrose diagram. Let x be the tortoise coordinate

$$x = r + 2M \ln \left| \frac{r}{2M} - 1 \right|, \quad (0 < x < \infty), \quad (\text{A2})$$

we can rewrite the metric as

$$ds^2 = f(r(x))(-dt^2 + dx^2) + r^2(x)g(r(x))d\Omega^2. (\text{A3})$$

Defining null coordinates,

$$\tan(V) = v = t + x, \quad \tan(U) = u = t - x, \quad (\text{A4})$$

on the interval $-\pi/2 < V < \pi/2$ and $-\pi/2 < U < \pi/2$, we can cover the entire spacetime at once, that is,

$$ds^2 = -\frac{f(r)dUdV}{\cos^2(U)\cos^2(V)} + \left(\frac{r}{x}\right)^2 \frac{g(r)\sin^2(V-U)}{4\cos^2(U)\cos^2(V)}d\Omega^2, \quad (\text{A5})$$

where r is defined in term of u and v as

$$\frac{1}{2}(v-u) = r + 2M \ln \left| \frac{r}{2M} - 1 \right|. \quad (\text{A6})$$

We now introduce a conformally related metric, $ds^2 = C_S^{-2}d\tilde{s}^2$, where conformal factor reads

$$C_S^{-2} = \frac{1}{4\cos^2(V)\cos^2(U)}. \quad (\text{A7})$$

The line element of conformal metric becomes

$$d\tilde{s}^2 = -4f(r)dUdV + \left(\frac{r}{x}\right)^2 g(r)\sin^2(V-U)d\Omega^2 (\text{A8})$$

Note that at the limit where $r \rightarrow 2M$, the line element is positive defined [$d\tilde{s}^2 > 0$].

The conformal spacetime is regarded as a manifold M with boundary ∂M : the coordinates are (U, V, θ, ϕ) with (θ, ϕ) the standard angular coordinates on the unit sphere and the boundary is the union of the sets future null infinity I^+ , past null infinity I^- , future timelike infinity i^+ , past timelike infinity i^- and spacelike infinity I^0 , defined by

$$\begin{aligned} I^+ &= \{(U, V, \theta, \phi) | U \in (-\pi/2, \pi/2), V = \pi/2\} \\ I^- &= \{(U, V, \theta, \phi) | V \in (-\pi/2, \pi/2), U = -\pi/2\} \\ i^\pm &= \{(U, V, \theta, \phi) | U = \pm\pi/2, V = \pm\pi/2\} \\ i^0 &= \{(U, V, \theta, \phi) | U = -\pi/2, V = \pi/2\} \end{aligned} \quad (\text{A9})$$

With this we can identify the different regions in the spacetime: i^0 , i^\pm and I^\pm . i^0 is the spacelike infinite that is, when $r \rightarrow \infty$ and t finite. i^\pm are the future and past timelike infinities, that is $t \rightarrow \pm\infty$ and r finite. Finally, I^\pm are the future null infinities ($t \rightarrow \infty$, $r \rightarrow \infty$ and rt finite) and past ($t \rightarrow -\infty$, $r \rightarrow \infty$ and $r+t$ finite). The Penrose diagram, with all regions, is drawn in the Fig.(36).

Null geodesics begin at a point of I^- and end at a point of I^+ . The timelike geodesics of the spacetime begin at i^- and end at i^+ , whereas spacelike geodesics start and end at i^0 .

Near the boundary, $r \rightarrow \infty$, then $r/x \rightarrow 1$ and consequently $f(r) \rightarrow 1$ and $g(r) \rightarrow 1$. In this way, the metric can be approximated by

$$ds^2 = -4dUdV + \sin^2(V-U)d\Omega^2. \quad (\text{A10})$$

Note that the null infinity of this solution is the same as the Schwarzschild black hole [3]. A point that not

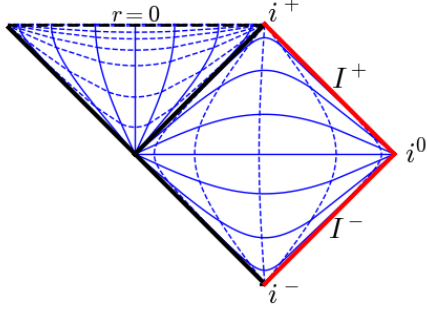


Figure 36: Penrose diagram for a dilatonic black hole, the bold red line corresponds to the event horizon whereas the dashed black line corresponds to the spacelike singularity.

always is true, specially for class of metric that are not asymptotically flat. The degenerate metric is obtained by taking $V = \pi/2$ and $dV = 0$ in above formula,

$$d\tilde{s}^2 = \cos^2(U)d\Omega^2. \quad (\text{A11})$$

This shows that I^+ is a null surface whose cross-sections ($U = \text{constant}$) are spheres of radii $\cos(U)$. This radius vanishes at i^0 and i^+ , showing that i^0 and i^+ (and similarly i^-) are points, not 2-spheres. Fig.(36) is a standard representation (Penrose diagram) of the conformal spacetime: the axis are $T = (U + V)/2$ and $X = (V - U)/2$, the coordinates (θ, ϕ) are suppressed, so every interior point in the diagram represents a sphere of radius $(\frac{x}{x} \sin(V - U))$. Points at $I^+(I^-)$ represent spheres of radii $\cos(U)(\cos(V))$, whereas i^0 and i^\pm represent actual points.

Remembering that the area of the sphere goes to zero when $r = Q^2/M$ and the surface is singular. Fig. (36) is plotted under the condition $Q^2 < 2M^2$, ensuring that the physical singularity is hidden by the event horizon.

For a particle moving in this spacetime, the Lagrangian for free particle is written as

$$\mathcal{L} = \frac{1}{2}g_{\mu\nu}\dot{x}^\mu\dot{x}^\nu. \quad (\text{A12})$$

In this case, the motion constants in the $\theta = \pi/2$ plane are

$$E = f\dot{t}, \quad L = \dot{\phi}r^2g(r) \quad (\text{A13})$$

Substituting (A13) in (A12), we arrive at one dimensional effective problem for the radial coordinate,

$$\dot{r}^2 = E^2 - f(r)\left(\frac{L^2}{r^2g(r)} + \epsilon\right) \quad (\text{A14})$$

where $\epsilon = 1, 0, -1$ for timelike, null and spacelike geodesics, respectively. Here the overdot means derivative with respect to proper time/affine parameter. The

effective potential is given by

$$V_{eff} = \left(\frac{L^2}{r^2\left(1 - \frac{Q^2}{Mr}\right)} + \epsilon - \frac{2ML^2}{r^3\left(1 - \frac{Q^2}{Mr}\right)} - \frac{2M\epsilon}{r} \right). \quad (\text{A15})$$

The effective potential has a positive constant term for $\epsilon = 1$ (timelike geodesics) as $r \rightarrow \infty$. Furthermore, considering $Q^2 < 2M^2$, the effective potential has a similar behavior to the Schwarzschild spacetime.

Appendix B: Logarithmic approximation for the backward glory effect

In this appendix, we are going to explore a different kind of approximation to determine the deflection angle (15). The main idea is to obtain a semi-analytic expression for the glory impact parameter b_g and its derivative. To do so, we consider the R.H.S of (13) for the critical impact parameter and determine its roots,

$$u_1 = u_c, \quad (\text{B1})$$

$$u_2 = \frac{4q^2u_c^2 - 2q^2u_c - 2u_c + 1 + \beta}{4(1 - 2q^2u_c)}, \quad (\text{B2})$$

$$u_3 = \frac{4q^2u_c^2 - 2q^2u_c - 2u_c + 1 - \beta}{4(1 - 2q^2u_c)}, \quad (\text{B3})$$

where the β -parameter is defined as

$$\beta = \left(16q^4u_c^4 - 16q^4u_c^3 + 4q^4u_c^2 + 16q^2u_c^3 - 4q^2u_c - 12u_c^2 + 4u_c + 1 \right)^{1/2}. \quad (\text{B4})$$

Putting all together, the function $h(u)$ reduces to cubic polynomial,

$$h(u) = (u - u_c)(u - u_2)(u - u_3) \quad (\text{B5})$$

Solving (15), we obtain that the deflection angle can be written in terms of elliptic integrals,

$$\Theta(b) \simeq -\frac{2}{\sqrt{u_2 - u_3}} \left(F(z, k) - K(k) \right), \quad (\text{B6})$$

where

$$k^2 = \frac{u_c - u_3}{u_2 - u_3}, \quad z^2 = \frac{u_3}{u_3 - u_c}. \quad (\text{B7})$$

In order to obtain the logarithmic deflection formula, we employ an approximation such that $k \simeq 1$ [29],

$$K(k) \simeq \frac{1}{2} \ln \left(\frac{16}{1 - k^2} \right), \quad F(z, k) = \frac{1}{2} \ln \left(\frac{1 + z}{1 - z} \right) \quad (\text{B8})$$

q	b_g/M	$\left. \frac{b_g^2}{M^2} \right _{\theta \sim \pi}$	$\left. \frac{db}{d\theta} \right _{\theta \sim \pi}$
0	5.35	4.85	
0.2	5.28	4.81	
0.4	4.95	4.55	
0.6	4.66	4.23	
0.8	3.96	3.54	
1	2.04	2.18	

Table II: Impact parameter for the glory effect using a logarithmic approximation for a dilatonic black hole.

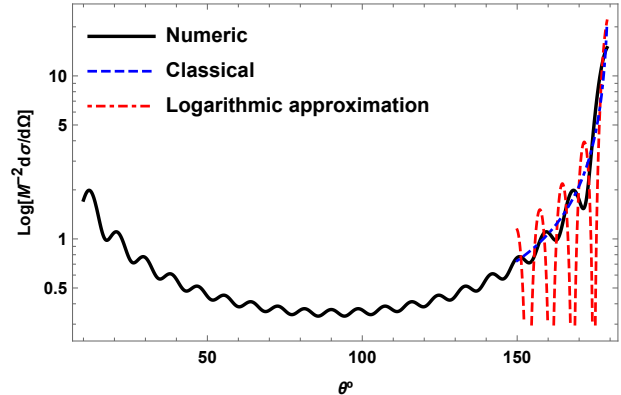


Figure 37: Numerical differential cross-section for the dilatonic black hole with $M\omega = 5$ and $q = 0.2$, the backward glory effect and the logarithmic approximation glory effect.

With the help of the above expression, the deflection angle (15) can be recast as

$$\Theta(b) \simeq -\frac{1}{\sqrt{u_2 - u_3}} \left[\ln \left(\frac{\sqrt{u_3 - u_c} + \sqrt{u_3}}{\sqrt{u_3 - u_c} - \sqrt{u_3}} \right) - \ln \left(\frac{16(u_2 - u_3)}{u_2 - u_c} \right) \right]. \quad (\text{B9})$$

Table(II) shows the values of the critical impact parameter using the logarithmic approximation. We obtain a small difference (nearly 1%) in relation with numerical integration results displayed in Tab.(I). In Figs. (37)-(37), we compare the full numerical differential scattering cross-section, the differential cross-section for the backward glory effect and the logarithmic approximation for the differential cross-section of the glory effect. Generally speaking, the logarithmic approximation is qualitatively good enough for describing the differential cross near 180° .

-
- [1] S. Chandrasekhar and K. S. Thorne. *The mathematical theory of black holes*. Oxford University Press, New York, 1985.
- [2] R. M. Wald. *General Relativity*. University of Chicago Press, 1984.
- [3] Frolov, Valeri and Novikov, Igor. *Black hole physics: basic concepts and new developments*. Springer Science & Business Media(2012).
- [4] Shipman, H. L.; Yu, Z; Du, Y.W. *The implausible history of triple star models for Cygnus X-1 Evidence for a black hole*. **Astrophysical Letters**, 16 (1): 9–12,1975.
- [5] F. Haardt et al. *Astrophysical Black Holes*. Springer, 2016.
- [6] B. P. Abbott et al. *Observation of Gravitational Waves from a Binary Black Hole Merger*. **Phys. Rev. Lett.** 116, 061102 (2016).
- [7] The Event Horizon Telescope Collaboration. *First M87 Event Horizon Telescope Results. I. The Shadow of the Supermassive Black Hole*. **The Astrophysical Journal Letters**, 875:L1 (17pp), 2019.
- [8] E. Cremmer, J. Scherk, and S. Ferrara. *SU(4) Invariant Supergravity Theory*. **Phys. Lett.** B74 (1978) 61-64.
- [9] S. Ferrara, R. Kallosh, and A. Strominger. *N=2 extremal black holes*. **Phys. Rev.** D52 (1995) 5412-5416.
- [10] S. Yu, J. Qiu and C.n Gao. *Constructing black holes in Einstein–Maxwell–scalar theory*. 2021 **Class. Quantum Grav.** 38 10500, Number 106.
- [11] M. Khodadi, A. Allahyari, S. Vagnozzi, D. F. Mota. *Black holes with scalar hair in light of the Event Horizon Telescope*. **JCAP** 2009 (2020) 026.

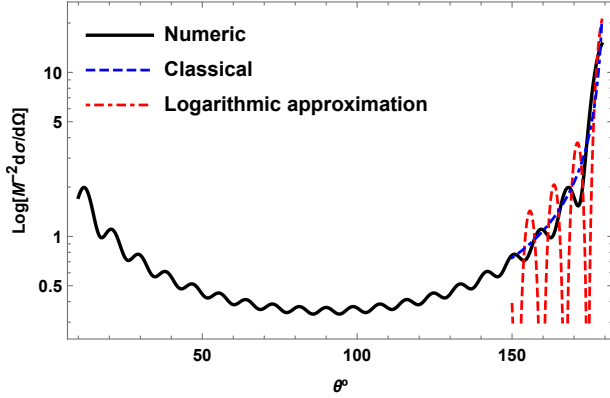


Figure 38: Numerical differential cross-section for the dilatonic black hole with $M\omega = 5$ and $q = 0.4$, the backward glory effect and the logarithmic approximation glory effect.

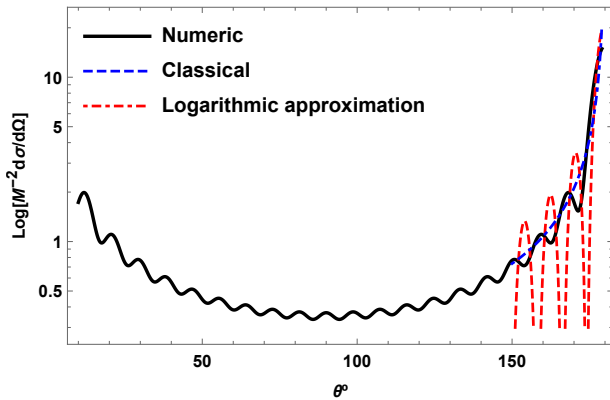


Figure 39: Numerical differential cross-section for the dilatonic black hole with $M\omega = 5$ and $q = 0.6$, the backward glory effect and the logarithmic approximation glory effect.

- [12] E. W. Hirschmann, L. Lehner, S. L. Liebling, and C. Palenzuela. “Black Hole Dynamics in Einstein-Maxwell-Dilaton Theory”. **Phys. Rev. D** 97, 064032 (2018).
- [13] M. Khalil, N. Sennett, J. Steinhoff, J. Vines, A. Buonanno. *Hairy binary black holes in Einstein-Maxwell-dilaton theory and their effective-one-body description*. **Phys. Rev. D** 98, 104010 (2018).
- [14] Félix-Louis Julié. *Gravitational radiation from compact binary systems in Einstein-Maxwell-dilaton theories*. **JCAP** 10(2018)033.
- [15] Félix-Louis Julié. *On the motion of hairy black holes in Einstein-Maxwell-dilaton theories*. **JCAP** 01(2018)026.
- [16] J. Jiang, B. Deng, and Z. Chen. *Static charged dilatonic black hole cannot be overcharged by gedanken experiments*. **Phys. Rev. D** 100, 066024 (2019).
- [17] T. Y. Yu and W. Y. Wen. *Cosmic censorship and Weak Gravity Conjecture in the Einstein–Maxwell-dilaton theory*. **Phys. Lett. B** 781, 713 (2018).
- [18] S. Chakraborty and S. SenGupta. *Solar system constraints on alternative gravity theories*. **Phys. Rev. D** 89, 026003 (2014).
- [19] W. Javed, J. Abbas, and A. Övgün. *Effect of the hair on deflection angle by asymptotically flat black holes in Einstein-Maxwell-dilaton theory*. **Phys. Rev. D** 100, 044052 (2019).
- [20] F. Rahaman, S. Molla, A. Ali, S. Ray. *Solar system tests in constraining parameters of dyon black holes*. **Eur. Phys. J. C** 78 (2018) 11, 948.
- [21] A. Tripathi, B. Zhou, A. B. Abdikamalov, D. Ayzenberg, and C. Bambi. *Constraints on Einstein-Maxwell dilaton-axion gravity from X-ray reflection spectroscopy*. **JCAP** 2107:002 (2021).
- [22] Matzner, Richard A. *Scattering of Massless Scalar Waves by a Schwarzschild “Singularity”*. **Journal of Mathematical Physics** 9.1(1968):163–170.
- [23] J.A.H. Futterman, F.A. Handler, R.A. Matzner. *Scattering from Black Holes*. Cambridge Monographs on Mathematical Physics (Cambridge University Press, Cambridge, 1988)
- [24] Sanchez, Norma. *Absorption and emission spectra of a Schwarzschild black hole*. **Physical Review D** 18.4(1978):1030.
- [25] Vishveshwara, CV. *Scattering of gravitational radiation by a Schwarzschild black-hole*. **Nature** 227.5261(1970):936–938.
- [26] Matzner, Richard A and DeWitte-Morette, Cécile and Nelson, Bruce and Zhang, Tian-Rong. *Glory scattering by black holes*. **Physical Review D** 31.8(1985):1869.
- [27] N. Andersson. *Scattering of massless scalar waves by a Schwarzschild black hole: A Phase integral study*. **Phys. Rev. D** 52 (1995) 4, 1808-1820.
- [28] Jung, Eylee and Park, DK. *Effect of scalar mass in the absorption and emission spectra of Schwarzschild black hole*. **Classical and Quantum Gravity** 21.15(2004):3717.
- [29] Crispino, Luís CB and Dolan, Sam R and Oliveira, Ednilton S. *Scattering of massless scalar waves by Reissner-Nordström black holes*. **Physical Review D** 76.6(2009):064022.
- [30] Crispino, Luís CB and Dolan, Sam R and Oliveira, Ednilton S. *Electromagnetic wave scattering by Schwarzschild black holes*. **Physical Review Letters** 102.23(2009):231103.
- [31] Dolan, Sam R and Oliveira, Ednilton S and Crispino, Luís CB. *Scattering of sound waves by a canonical acoustic hole*. **Physical Review D** 79.6(2009):064014.
- [32] Benone, Carolina L and de Oliveira, Ednilton S and Dolan, Sam R and Crispino, Luís CB. *Absorption of a massive scalar field by a charged black hole*. **Physical Review D** 89.10(2014):104053.
- [33] Carolina L. Benone, Ednilton S. de Oliveira, Sam R. Dolan, Luis C. B. Crispino. *Addendum to “Absorption of a massive scalar field by a charged black hole”*. **Phys. Rev. D** 95, 044035 (2017).
- [34] Macedo, Caio FB and Leite, Luiz CS and Crispino, Luís CB. *Absorption by dirty black holes: null geodesics and scalar waves*. **Physical Review D** 93.2(2016):024027.
- [35] Leite, Luiz CS and Dolan, Sam R and Crispino, Luís CB. *Scattering of massless bosonic fields by Kerr black holes: On-axis incidence*. **Physical Review D**

- 100.8(2019):084025.
- [36] Huang, Yang and Zhang, Hongsheng. *Scattering of massless scalar field by charged dilatonic black holes*. **European Physical Journal C** 80.7(2020):1–13.
- [37] Liao, Hao and Chen, Juhua and Wang, Yongjiu. *Scattering of scalar wave from black hole Hovara-Lifshitz gravity*. **International Journal of Modern Physics D** 21.05(2012):1250045.
- [38] A. Delhom, C. F. B. Macedo, G. J. Olmo, Luís C. B. Crispino. *Absorption by black hole remnants in metric-affine gravity*. **Phys.Rev.D** 100 (2019) 2, 024016.
- [39] Décanini, Yves and Folacci, Antoine and Jensen, Bruce. *Complex angular momentum in black hole physics and quasinormal modes*. **Physical Review D** 67.12(2003):124017.
- [40] Décanini, Yves and Folacci, Antoine. *Regge poles of the Schwarzschild black hole: A WKB approach*. **Physical Review D** 81.2(2010):024031.
- [41] Décanini, Yves and Esposito-Farese, Gilles and Folacci, Antoine. *Universality of high-energy absorption cross-sections for black holes*. **Physical Review D** 83.4(2011):044032.
- [42] Décanini, Yves and Folacci, Antoine and Bernard, Raffaelli. *Fine structure of high-energy absorption cross-sections for black holes*. **Class. Quantum Grav.** 28 175021 (2011).
- [43] R. Brito, V. Cardoso and P. Pani. *Superradiance*. **Lecture Notes in Physics** 971 (2020). [arXiv:1501.06570].
- [44] Benone, Carolina L and Crispino, Luís CB. *Superradiance in static black hole spacetimes*. **Physical Review D** 93.2(2016):024028
- [45] Gibbons, Gary W and Maeda, Kei-ichi. *Black holes and membranes in higher-dimensional theories with dilaton fields*. **Nuclear Physics B** 298.4(1988):741–775.
- [46] Garfinkle, David and Horowitz, Gary T and Strominger, Andrew. *Charged black holes in string theory*. **Physical Review D** 43.10(1991):3140.
- [47] Li, Ran. *Stability of charged black holes in string theory under charged massive scalar perturbations*. **Physical Review D** 88.12(2013):127901.
- [48] Gonzalez, PA and Olivares, Marco and Papantonopoulos, Eleftherios and Vásquez, Yerko. *Motion and collision of particles in a rotating linear dilaton black hole*. **Physical Review D** 97.6(2018):064034.
- [49] Olver, Frank WJ and Lozier, Daniel W and Boisvert, Ronald F and Clark, Charles W. *NIST handbook of mathematical functions hardback and CD-ROM*. Cambridge university press(2010)
- [50] Abramowitz, Milton and Stegun, Irene A and Romer, Robert H. *Handbook of mathematical functions with formulas, graphs, and mathematical tables*. American Association of Physics Teachers(1988)
- [51] K. W. Ford and J. A. Wheeler. *Semiclassical description of scattering*. **Ann. Phys.** (N.Y.) 7, 259 (1959).
- [52] Cássio I.S. Marinho and E. S. de Oliveira. *Scattering of massless scalar waves from schwarzschild-tangherlini black holes on the brane*. [arXiv:1612.05604].
- [53] Carolina L. Benone and Luís C.B. Crispino. *Massive and charged scalar field in Kerr-Newman spacetime: Absorption and superradiance*. **Phys.Rev.D** 99 (2019) 4, 044009.
- [54] Chris Doran, Anthony Lasenby, Sam Dolan, and Ian Hinder. *Fermion absorption cross-section of a Schwarzschild black hole*. **Physical Review D** 71, 124020 (2005).
- [55] Cardoso, Vitor and Miranda, Alex S and Berti, Emanuele and Witek, Helvi and Zanchin, Vilson T. *Geodesic stability, Lyapunov exponents, and quasinormal modes*. **Physical Review D** 79.6(2009):064016.
- [56] Hui, Lam and Ostriker, Jeremiah P and Tremaine, Scott and Witten, Edward. *Ultralight scalars as cosmological dark matter*. **Physical Review D** 95.4(2017):043541.
- [57] Miller-Jones, James C. A.; et al. "Cygnus X-1 contains a 21-solar mass black hole—Implications for massive star winds". **Science**. 371 (6533): 1046–1049. arXiv:2102.09091.
- [58] J. E. Greene, J. Strader, and L. C. Ho. *Intermediate-Mass Black Holes*. **Annual Reviews** Vol. 58:257-312. [https://doi.org/10.1146/annurev-astro-032620-021835]
- [59] D. R. Wilkins, L. C. Gallo, E. Costantini, W. N. Brandt & R. D. Blandford. *Light bending and X-ray echoes from behind a supermassive black hole*. **Nature** V595, 657–660 (2021).
- [60] McConnell, N. et al. *Two ten-billion-solar-mass black holes at the centres of giant elliptical galaxies*. **Nature**. 480 (7376): 215–8, (2011). [arXiv:1112.1078].
- [61] K. Kadota, T. Sekiguchi, H. Tashiro. *A new constraint on millicharged dark matter from galaxy clusters*. [arXiv:1602.04009]
- [62] A. Stebbins and G. Krnjaic. *New Limits on Charged Dark Matter from Large-Scale Coherent Magnetic Fields*. [arXiv:1908.05275].
- [63] J.B. Muñoz and A. Loeb. *A small amount of mini-charged dark matter could cool the baryons in the early Universe*. **Nature** V557, 684–686 (2018).
- [64] K. Kohri and T. Terada. *Solar-mass primordial black holes explain NANOGrav hint of gravitational waves*. **Physics Letters B** 813 (2021) 136040,
- [65] J. M. Bardeen, W. H. Press, and S. A. Teukolsky. *Rotating Black Holes: Locally Nonrotating Frames, Energy Extraction, and Scalar Synchrotron Radiation*. **Astrophys.J.** 178, 347 (1972).
- [66] W. H. Press and S. Teukolsky. *Floating Orbits, Superradiant Scattering and the Black-hole Bomb*. **Nature** (London) 238, 211 (1972).
- [67] V. Cardoso, O.J.C. Dias, J. P.S. Lemos, and S. Yoshida. *Black-hole bomb and superradiant instabilities*. **Phys.Rev. D** 70(4):044039, 2004.
- [68] P. Pani, V. Cardoso, L. Gualtieri, E. Berti, and A. Ishibashi. *Black-Hole Bombs and Photon-Mass Bounds*. **Phys. Rev. Lett.** 109, 131102 (2012).
- [69] A. Arvanitaki and S. Dubovsky. *Exploring the string axiverse with precision black hole physics*. **Phys. Rev. D** 83, 044026 (2011).
- [70] R. A. Konoplya. *Superradiant instability for black holes immersed in a magnetic field*. **Phys.Lett.B** 666:283-287 (2008); **Phys.Lett.B** 670:459 (2009).
- [71] J. C. Degollado, C. Herdeiro, and H. F. Runarsson. *Rapid growth of superradiant instabilities for charged black holes in a cavity* **Phys.Rev. D** 88, 063003 (2013).
- [72] S. Hod. *Stability of the extremal Reissner–Nordström black hole to charged scalar perturbations*. **Phys. Lett.**

- B** 713 (2012) 505.
- [73] S. Hod. *No-bomb theorem for charged Reissner-Nordström black holes*. **Phys. Lett. B** 718 (2013) 1489.
- [74] S. Hod. *Stability of highly-charged Reissner-Nordström black holes to charged scalar perturbations*. **Phys. Rev. D** 91 (2015) 044047.
- [75] S. Hod. *The charged black-hole bomb: A lower bound on the charge-to-mass ratio of the explosive scalar field*. **Phys. Lett. B** 755 (2016) 177–182.
- [76] N. Sanchis-Gual *et al.*. *Explosion and Final State of an Unstable Reissner-Nordström Black Hole*. **Phys.Rev. Lett.** 116, 141101 (2016).
- [77] Y. Huang, D. J. Liu, X. H. Zhai, and X. Z. Li. *Massive charged Dirac fields around Reissner-Nordström black holes: Quasibound states and long-lived modes*. **Phys. Rev. D** 96, 065002 (2017).
- [78] Y. Huang, D. J. Liu, and X. Z. Li. *Instability for massive scalar fields in Kerr-Newman spacetime*. **Phys. Rev. D** 98, 025021 (2018).
- [79] Y. Huang, D. J. Liu, and X. Z. Li. *Superradiant instability of D -dimensional Reissner–Nordström–anti-de Sitter black hole mirror system*. *Int. J. Mod. Phys. D.* 26, 1750141 (2017).
- [80] R. Li. *Stability of charged black holes in string theory under charged massive scalar perturbations*. **Phys. Rev. D** 88, 127901 (2013).
- [81] R. Li and J. Zha. *Superradiant instability of the charged scalar field in stringy black hole mirror system*. **The European Physical Journal C** V.74, 3051 (2014).
- [82] G. W. Gibbons. *Vacuum polarization and the spontaneous loss of charge by black holes*. **Commun. Math. Phys.** 44, 245–264 (1975).
- [83] V. Cardoso, C. F. B. Macedo, P. Pani, and V. Ferrari. *Black holes and gravitational waves in models of minicharged dark matter*. **JCAP** 1605, 054 (2016).
- [84] A. Urbano. *Towards a proof of the Weak Gravity Conjecture*. [arXiv:1810.05621].
- [85] J. Y. J. Burton and T. Osburn. *Reissner-Nordström perturbation framework with gravitational wave application*.
- [86] J.M. Fernández Tío, G. Dotti. *Black hole nonmodal linear stability: odd perturbations of Reissner-Nordström*. **Phys. Rev. D** 95, 124041 (2017).
- [87] G. Dotti and J.M. Fernández Tío. *Black hole nonmodal linear stability: even perturbations in the Reissner-Nordström case*. **Phys. Rev. D** 101, 024034 (2020).